Regional Studies in Marine Science 69 (2024) 103325

Contents lists available at ScienceDirect

Regional Studies in Marine Science

journal homepage: www.elsevier.com/locate/rsma

Upwellings and downwellings on the edge of the Gaspé Current: Observations and processes☆

Théau Leclercq [a,1], Cédric Chavanne [a,*,2], Pierre Larouche [b,3]

[a] Université du Québec à Rimouski - Institut des sciences de la mer de Rimouski (UQAR-ISMER), 310 Allée des Ursulines, Rimouski, G5L2Z9, Québec, Canada
[b] Fisheries and Oceans Canada - Maurice Lamontagne Institute, 850 Route de la Mer, Mont-Joli, G5H3Z4, Québec, Canada

ARTICLE INFO

Dataset link: https://doi.org/10.26071/ogsl-9acdc006-20cb, https://catalogue.preprod.ogsl.ca/dataset/ca-cioos_9acdc006-20cb-4c7e-8aae-ca1007cf9b63, https://ogsl.ca/en/satellite-remote-sensing-data-information/, https://ogsl.ca/en/satellite-remote-sensing-application/, Click here to access CTD V-FIN data, https://cds.climate.copernicus.eu/cdsapp#!/dataset/reanalysis-era5-single-levels?tab=overview

Keywords:
Gaspé Current
Upwelling
Downwelling
Water masses analysis
Frontogenesis
Frontolysis
Nonlinear Ekman pumping

ABSTRACT

The Gaspé Current carries the relatively fresh surface waters of the St. Lawrence estuary along the Gaspé peninsula to the Gulf of St. Lawrence. It presents complex dynamics including the development of meanders. A density front separates the fresher surface waters of the estuary from the saltier surface waters of the gulf. Over the past 40 years, upwellings and downwellings observed on the edge of this front have been the subject of several investigations. Tang (1982) proposed an analytical model featuring a permanent circulation consisting of an upwelling offshore of the front and a downwelling below the front. Using a unique set of *in situ* observations made with CTD (Conductivity Temperature Depth) profilers and ADCP (Acoustic Doppler Current Profiler) data collected between September 1991 and June 1993, upwellings and downwellings were inferred using a water masses analysis. Even if their presence is predominant (~ 80% of the total number of sampled transects), they are not a permanent feature over the entire length of the Gaspé Current front, and their positions relative to the front vary. This data set also made it possible to determine via the ω equation that these vertical currents mostly result from frontogenesis and frontolysis (strengthening and weakening of the front). A new method to combine the ω equation with the nonlinear Ekman pumping shows that wind-driven vertical motions were generally weaker and much shallower than those due to frongenesis/frontolysis. This analysis shows that upwellings and downwellings are dependent on favorable conditions leading to the establishment of Gaspé Current instabilities and to frontogenesis or frontolysis.

1. Introduction

The Gaspé Current is an important surface circulation feature in the northwestern Gulf of St. Lawrence, originating at the end of the lower estuary (near Pointe-des-Monts) and extending to the Magdalen Islands. Its formation is the result of the relatively-fresh water outflow from the St. Lawrence estuary along the south shore (Fig. 1). Occasionally, this outflow is complemented by an episodic current along the estuary's north shore that veers southward along a salinity front south of Pointe-des-Monts (Mertz et al., 1992; Sheng, 2001). Downstream, the Gaspé Current is then intensified by the cyclonic Anticosti Gyre. Its main characteristics are: a depth that can reach 40 m, a velocity that can exceed 1 m s^{-1} in the summer and a width that can reach 20 km. These characteristics also vary seasonally. Being driven by salinity gradients, one of the main feature of the Gaspé current is a front along its northern edge that separates coastal brackish waters from saltier waters of the northwestern Gulf of St. Lawrence (Benoit et al., 1985).

The first survey of the Gaspé Current was realized in 1895 by William Bell Dawson, a pioneer local hydrographer whose conclusion about the dynamics of this current was that it was regulated by astronomical forcing (Farquharson, 1962). More recent research about the dynamics of the Gaspé Current have shown that it is actually a buoyancy-driven coastal jet subject to baroclinic instabilities causing meanders of its front (Mertz et al., 1988; Sheng, 2001).

☆ The writing of this paper is based on the master's thesis of Théau Leclercq (first author) published in the digital library of the Université du Québec à Rimouski (UQAR) in March 2022: ©Master's thesis of Théau Leclercq. It has not yet been published in a peer-reviewed journal.

* Correspondence to: ISMER, 310 Allée des Ursulines, Rimouski, QC 5L 2Z9, Québec, Canada.
E-mail addresses: theau.leclercq@cidco.ca (T. Leclercq), Cedric_Chavanne@uqar.ca (C. Chavanne), pierre.larouche@dfo-mpo.gc.ca (P. Larouche).
URLs: https://cidco.ca/en/theau-leclercq (T. Leclercq), https://www.ismer.ca/recherche/equipe/chavanne-cedric (C. Chavanne), https://profils-profiles.science.gc.ca/en/profile/pierre-larouche (P. Larouche).

[1] Théau Leclercq graduated from his master's degree in physical oceanography at the UQAR-ISMER in March 2022.
[2] Cédric Chavanne is a professor in physical oceanography at the UQAR-ISMER.
[3] Pierre Larouche is an emeritus researcher in oceanography and teledetection at the Maurice Lamontagne Institute.

https://doi.org/10.1016/j.rsma.2023.103325
Received 9 August 2023; Received in revised form 1 December 2023; Accepted 6 December 2023
Available online 10 December 2023

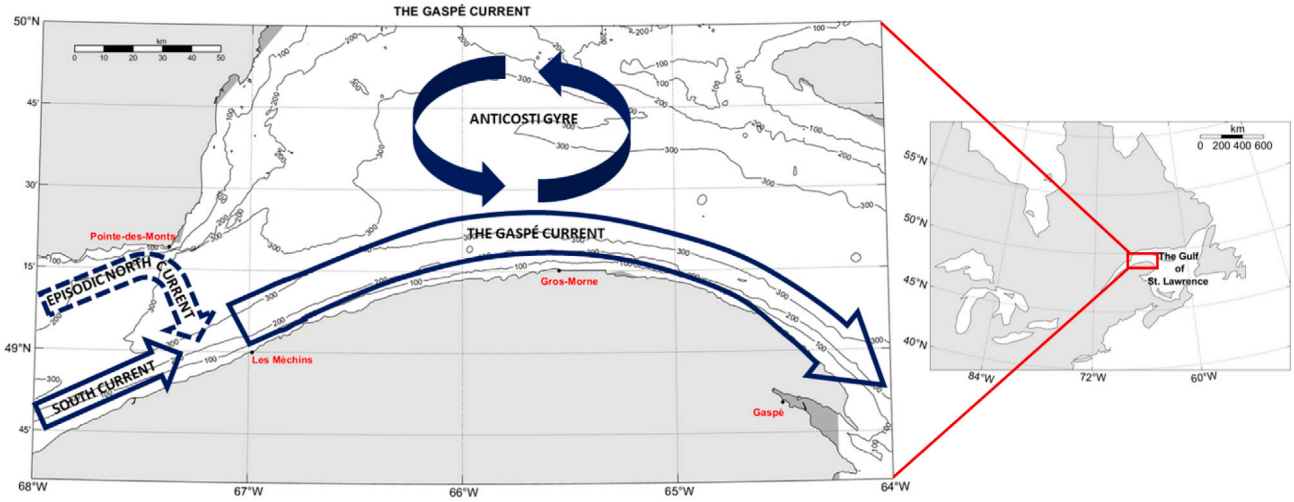

Fig. 1. The study area: the Gaspé Current (located in the northwestern Gulf of St. Lawrence).

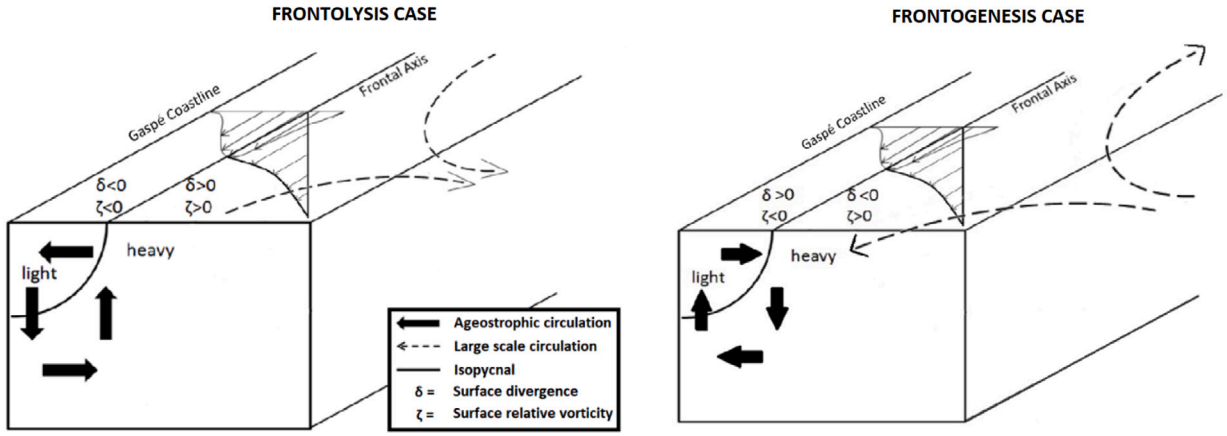

Fig. 2. Schematization of frontolysis and frontogenesis (Hoskins and Bretherton, 1972) modified from McWilliams et al. (2009) and adapted to the Gaspé Current front area.

In this context, upwellings and downwellings near the front have been a subject of research for 40 years. Observations showed a minimum of temperature near the front for some CTD transects leading to the proposal of an analytical model to explain vertical currents (Tang, 1982, 1983). The interfacial Ekman transport associated with a front was the hypothesis put forward to explain upwellings and downwellings on the edge of the Gaspé Current. Horizontal density gradients create vertical shears, through thermal-wind balance, causing an interfacial Ekman transport under the front (permanent downwelling) while offshore of the front, a permanent upwelling is created. This model has however never been fully tested using *in situ* data, and does not consider the effect of wind-driven nonlinear Ekman transport (Stern, 1965) nor the effect of the Gaspé front meanders which could lead to frontogenesis or frontolysis (Hoskins and Bretherton, 1972). Frontogenesis or frontolysis leads to intensification or weakening of a front. When a front in quasi-geostrophic equilibrium is subjected to straining by background currents, an ageostrophic circulation involving vertical currents develops to restore the geostrophic equilibrium (Fig. 2). The upwellings present along the Gaspé Current front could also be generated by nonlinear Ekman transport due to the relative vorticity of the Gaspé Current (Stern, 1965; Niiler, 1969). Upwellings are caused by the divergence of the nonlinear Ekman transport created by westerly winds and downwellings by easterly winds (Fig. 3).

In light of the above-mentioned limitations of the frontal model proposed by Tang (1982), this paper addresses the following questions: are vertical motions present along the Gaspé current and what are the main physical mechanisms causing upwellings and downwellings near the Gaspé Current front?

2. Data and methods

2.1. Data

Between 1991 and 1993, four cruises were carried out in the Gaspé Current to collect high resolution hydrographic data (Larouche, 1993a,b,c,d, 2023) between Les Méchins and Gros-Morne where the current is the fastest. These cruises were designed to evaluate the possibility to detect horizontal surface shears of the Gaspé Current using ERS-1 (European Remote-Sensing Satellite 1) synthetic aperture radar images (Larouche, 1996). These high spatial resolution hydrographic data will be used to diagnose vertical motions near the Gaspé Current front. They consist of 12 transects (with some repetitions) for each cruise realized respectively in September 1991, May 1992, July/August 1992, and June 1993 (Fig. 4). During the first three cruises, conductivity, temperature and depth data were acquired at a grid of stations with a Guildline 8715 CTD, while currents data were acquired along each transect continuously with Teledyne RDI Workhorse ADCPs (Acoustic Doppler Current Profilers). During Cruise 4 (June 1993), vertically oscillating CTD data (ENDECO V-FIN System, Model 1074) were collected along each transect simultaneously with the ADCP. This technique is a continuous acquisition of temperature

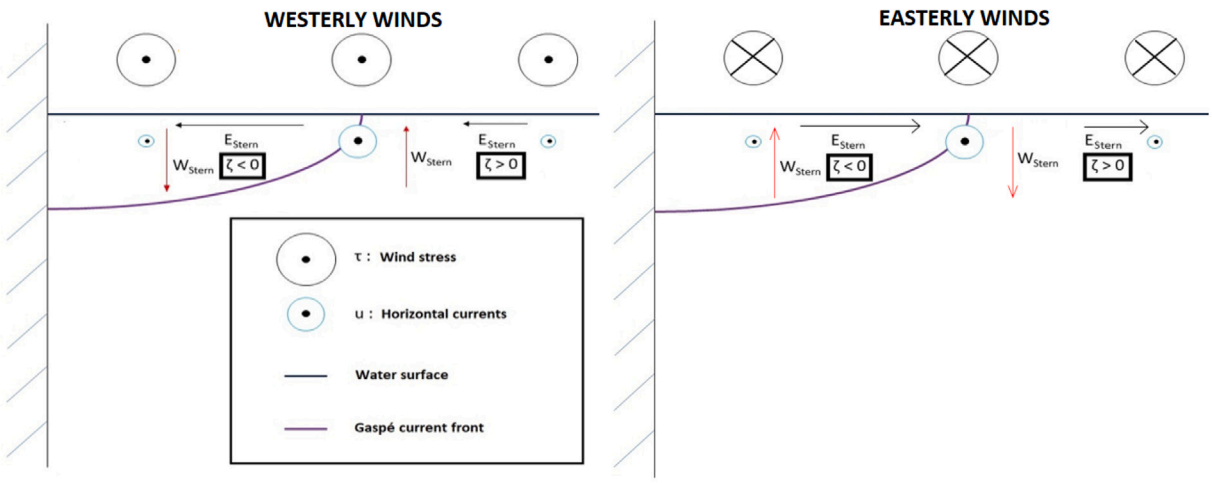

Fig. 3. Schematization of nonlinear Ekman transport (Stern, 1965) adapted to the Gaspé Current front area with westerly winds (left) and easterly winds (right).

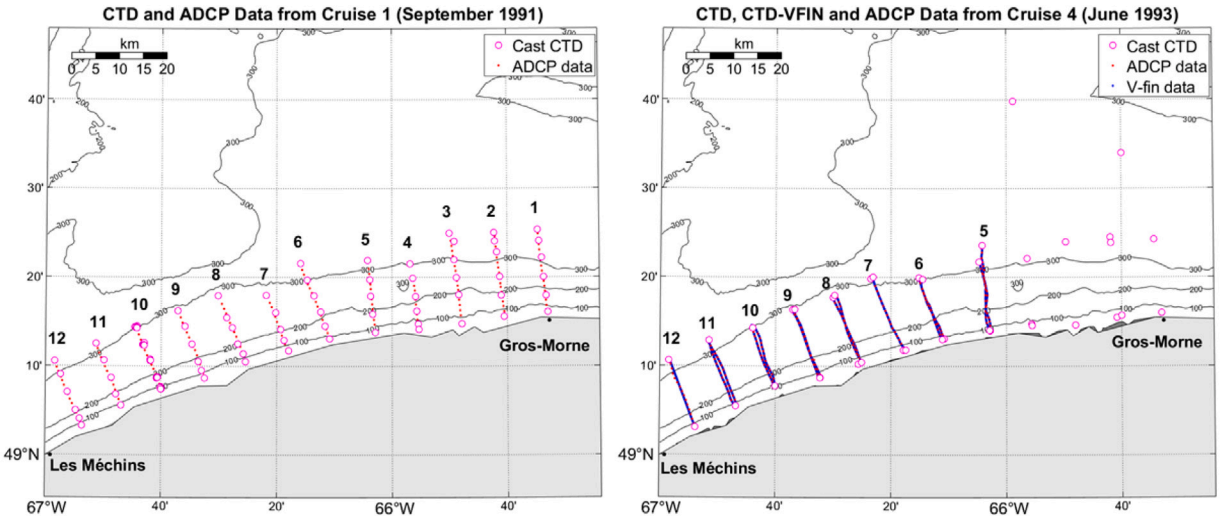

Fig. 4. Cruise 1 (September 1991) and Cruise 4 (June 1993): localization of the 12 transects of CTD casts, ADCP data and the 8 transects of CTD V-FIN.

and salinity data with a sawtooth pattern (V-shape) in the water column to study small-scale variability with better horizontal resolution. The CTD V-FIN system acquisition rate was 1 Hz, its averaged horizontal velocity was 1.48 m s^{-1}, and its averaged vertical velocity, 0.18 m s^{-1}. The difference in resolution between CTD casts and CTD V-FIN data has been tested by creating synthetic CTD casts from CTD V-FIN objectively-interpolated data, showing that major upwellings and downwellings can be inferred with the lower CTD casts resolution (see Appendix A.1).

Raw CTD data (including CTD V-FIN profiles), were processed using standard quality control procedures (Sea-Bird, 2017) including removing pressure loops. Conservative temperature, absolute salinity, and seawater density were computed using the TEOS-10 algorithms (McDougall and Barker, 2011).

The ship-borne ADCP (150 kHz for the first cruise, and 600 kHz for the other three) was operated with bottom-tracking during Cruise 1 to correct the measured water velocities for the motion of the ship. A temporal averaging over 6 min and 30 s, corresponding to an average horizontal resolution close to 1000 m, was performed to reduce measurement noise. Unfortunately, bottom tracking was not possible during Cruise 2 to 4 due to the higher frequency of the ADCP used to increase the vertical resolution of the currents, at the expense of the accuracy of barotropic currents. Ship GPS data was used to compute the ship velocity, but the accuracy was insufficient to properly remove the ship motion from the water velocity data due to the positioning method (non-differential GPS), the presence of Selective Availability (SA) before May 2000 (Adrados et al., 2002) and less satellite coverage in the 1990s. The position accuracy was ~ 10 m, and the resulting of horizontal currents was ~ 0.1 m s^{-1}. Since water velocity is required to test the different mechanisms that could cause vertical currents, these tests will be performed only for Cruise 1. Data near the bottom biased by side-lobes reflection were discarded.

Daily sea-surface temperature (SST) data were obtained from the St. Lawrence Global Observatory (SLGO) using AVHRR (Advanced Very-High-Resolution Radiometer) satellite sensors with a resolution of 1 km. Wind data (the velocity at 10 m above the sea surface) were obtained from reanalyzes produced by the ERA5 model available from ECMWF (The European Center for Medium-Range Weather Forecasts). The temporal resolution is 1 h and the spatial resolution is a 0.25° x 0.25° grid.

2.2. Characterization of the frontal zone

Since CTD stations were not regularly spaced along each transect, salinity, temperature, and density were objectively-interpolated (Bretherton et al., 1976) on a regularly-spaced 2-D (depth, distance) grid for each transect. The horizontal decorrelation scale was chosen to be the average first baroclinic deformation radius, computed at each

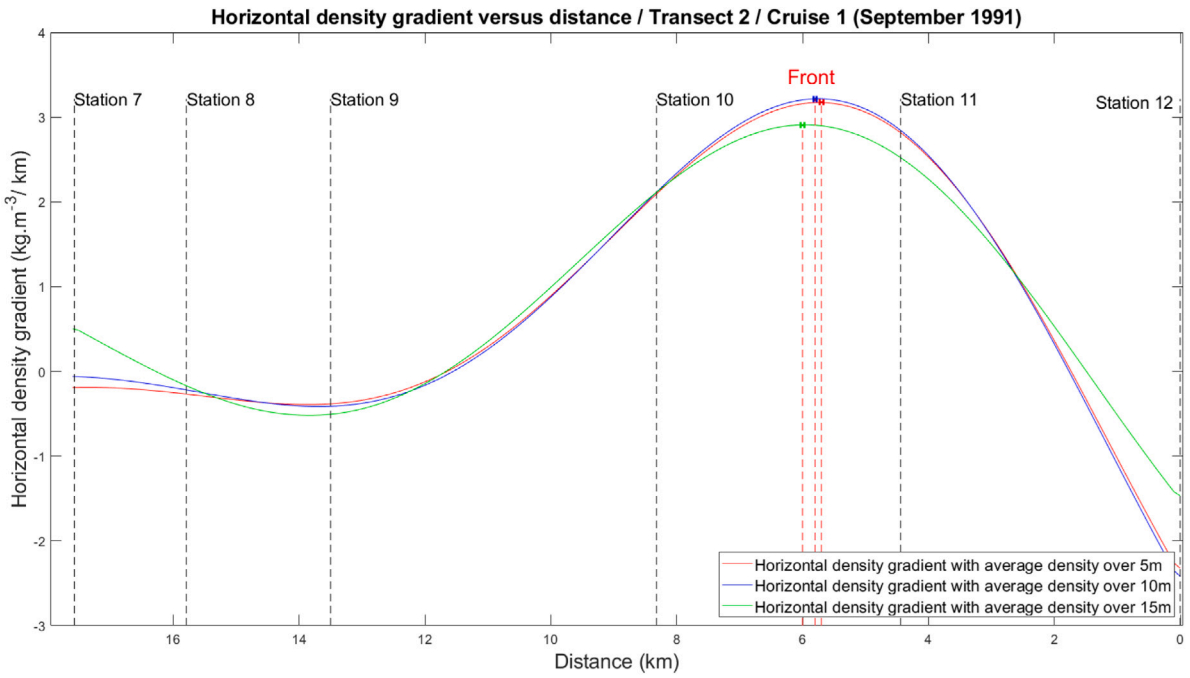

Fig. 5. Example of horizontal density gradient versus the distance along transect 2 of Cruise 1 (September 1991) to localize the Gaspé Current front (maximum absolute value of the gradient) with its estimated uncertainty (horizontal error bars).

CTD station (Chelton et al., 1998). The vertical decorrelation scale was chosen to be the smallest value of the vertical auto-correlation function zero-crossing for temperature, salinity, or density computed at each CTD station. Referring to instrumental error, the noise level is assumed to be 5.10^{-3} °C for temperature and 5.10^{-3} g/kg for absolute salinity. The density is calculated from temperature and salinity with TEOS-10 algorithms at each CTD station, and then objectively-interpolated. In Fig. 5a, the standard error of the interpolated density is calculated with the propagation of uncertainty (Thomson and Emery, 2014):

$$\sigma_\rho^2 = \frac{\partial \rho}{\partial \mathrm{T}}^2 .\sigma_\mathrm{T}^2 + \frac{\partial \rho}{\partial \mathrm{S}}^2 .\sigma_\mathrm{S}^2, \tag{1}$$

where ρ is the density, T the temperature and S the salinity. By linearizing the equation of state, we obtain :

$$\frac{\partial \rho}{\partial \mathrm{T}} = -\alpha.\rho_0 \tag{2}$$

$$\frac{\partial \rho}{\partial \mathrm{S}} = -\beta.\rho_0 \tag{3}$$

where α is the coefficient of thermal expansion, β the haline contraction coefficient, and ρ_0 the average density of the water column. α and β are computed using TEOS-10 algorithms.

The position of the front is defined as the distance from the CTD station closer to shore of the horizontal density gradient maximum absolute value, where density has been averaged over a 10 m depth from the sea surface (depths of 5 and 15 m were also tested yielding similar positions, see Fig. 5).

To estimate uncertainties of the front positions, the first step is to average the standard error of the interpolated density over the length of the transect and the depth between the surface and the maximum depth of the isopycnal that defines the front. The resulting density error is called $\sigma_{\rho e}$. The next step is to determine the horizontal distance and the maximum depth of the front isopycnal $\sigma_{\rho F} \pm \sigma_{\rho e}$. The differences in front distance and the maximum depth yield the resulting uncertainties. The uncertainties for the front distance are shown in Fig. 5, and are much smaller than the differences in front position due to the choice of the depth averaging interval from the surface (5 m, 10 m or 15 m).

2.3. Analysis of water masses

The effects of upwellings and downwellings on the distribution of water masses across a density front are best visualized by estimating the percentages of different water masses mixed together across the front. As many water masses as there are conserved properties measured can be determined. Gasparin et al. (2014) used the same method to determine and differentiate the water masses inside the Coral Sea. Here, neglecting surface heat and freshwater fluxes, we use conservation of temperature, salinity, and mass to determine the percentages of up to three water masses within each CTD transect. Although there are more than three water masses present, we restrict our analysis to the three least dense water masses (Eqs. (4),(5),(6)). Once the water masses have been defined (see Section 3.2), their percentages X_i (i = 1, 2, 3) can be computed for each data point lying in the "mixing triangle" (Fig. 6) by solving the linear system of equations:

$$\mathrm{T} = \mathrm{T}_1 X_1 + \mathrm{T}_2 X_2 + \mathrm{T}_3 X_3 \tag{4}$$

$$\mathrm{S} = \mathrm{S}_1 X_1 + \mathrm{S}_2 X_2 + \mathrm{S}_3 X_3 \tag{5}$$

$$1 = X_1 + X_2 + X_3 \tag{6}$$

The percentage of each water mass is then optimally-interpolated similarly to the CTD data.

2.4. Diagnosing vertical velocities

2.4.1. Frontogenesis and frontolysis

The ω equation (Eq. (7)) is a 3D partial differential equation developed by Hoskins et al. (1978). It is used to calculate vertical currents in the case of frontogenesis/frontolysis (Pinot et al., 1996) with $\boldsymbol{Q}$ (Eq. (8)) corresponding to the geostrophic forcing:

$$\nabla^2(N^2\mathrm{w}) + f^2 \frac{\partial^2 \mathrm{w}}{\partial z^2} = 2\boldsymbol{\nabla}.\boldsymbol{Q}, \tag{7}$$

$$\boldsymbol{Q} = (Q_x, Q_y) = \frac{g}{\rho_0}\left(\frac{\partial \boldsymbol{u_g}}{\partial x}.\boldsymbol{\nabla}\boldsymbol{\rho}, \frac{\partial \boldsymbol{u_g}}{\partial y}.\boldsymbol{\nabla}\boldsymbol{\rho}\right), \tag{8}$$

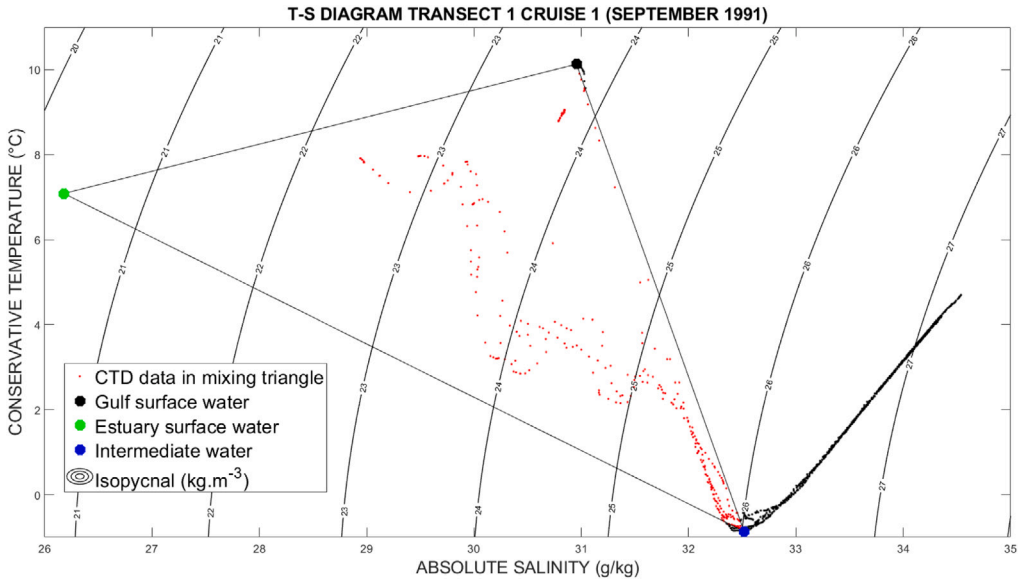

Fig. 6. Mixing triangle using three reference water masses to determine the percentage of each water mass for all CTD data contained in the mixing triangle (red dots). (For interpretation of the references to color in this figure legend, the reader is referred to the web version of this article.)

where N is the Brunt–Väisälä frequency, w the vertical currents, f the Coriolis parameter, $\boldsymbol{u_g}$ the horizontal absolute geostrophic currents, ρ_0 the average density of the area and ρ the density. The $\boldsymbol{\omega}$ equation has been generalized to account for ageostrophic forcing (Viúdez et al., 1996; Giordani et al., 2006). However, we will restrict our analysis to the first order geostrophic forcing $\boldsymbol{Q}$.

Here, the method to calculate vertical currents using the $\boldsymbol{\omega}$ equation relies upon the work of Rudnick (1996) where he studied vertical currents of the Azores front. The first step is to remove all density overturns using a least squares method with a constraint $\frac{\partial \rho}{\partial z} \leqslant 0$ (Lawson and Hanson, 1995), since density overturns in the omega equation lead to aberrant values of w. In a second step, Rudnick (1996) calculated absolute geostrophic currents using both vertical geostrophic shear obtained with density data from CTD casts and horizontal velocities (u and v) from ADCP data (see Appendix A.2). To do so, he used a stream function $\psi\ (x, y)$ and interpolated density and horizontal currents for each depth on a 2D grid (horizontal plane). Hence, geostrophic currents which could be calculated with just CTD casts differ from absolute geostrophic currents needing both ADCP data and CTD casts. In contrast, we use a 3D interpolation with a smoothness constraint (Nicholson, 2021), which approaches an optimal 3D interpolation and avoids a vertical decorrelation of interpolated data that can occur using Rudnick's method. Considering the unstable behavior of the Gaspé Current, we only interpolate three consecutive CTD and ADCP transects in time and space (e.g., transects number 1,2,3, or 2,3,4) to perform this 3D interpolation. The interpolation grid has a resolution of dx = 200 m, dy = 200 m and dz = 1 m. The size of the grid is 100 × 150 × 75. The values chosen for the smoothness parameter are 10^{-3} for CTD and 10^{-2} for ADCP data and reflect the accuracy of the measurements: the higher the noise, the higher the smoothness parameter should be.

We solve the $\boldsymbol{\omega}$ equation using SOR (Successive Over Relaxation) method, specifically the Jacobi relaxation method (Press et al., 1992), which is particularly useful for speeding up calculation time. The boundary condition at the surface is w = 0 m s^{-1}, but the lateral and bottom boundary conditions must be chosen arbitrarily. Following (Rudnick, 1996), we push the lateral and bottom boundaries far away from the region of interest (i.e. 5 km away in the north/south direction, 10 km away in the east/west direction due to the interpolation of 3 consecutive transects, and 75 m away in the vertical) and use either w = 0 (Dirichlet) or $\frac{\partial w}{\partial n} = 0$ (Neumann, where n is the normal to the boundary), resulting in variations in the solution of less than 2%. Differences between Dirichlet and Neumann boundary conditions are shown in Appendix A.3.

The uncertainty of vertical currents is calculated by repeating 20 times the calculation of the $\boldsymbol{\omega}$ equation with slightly modified horizontal velocities and density fields. These fields are modified by adding vertically non-correlated errors taken from a normal distribution with a standard deviation of 10^{-2} kg m^{-3} for density, and vertically correlated errors taken from a normal distribution with a standard deviation of 3.10^{-2} m s^{-1} for horizontal velocities, which represent bottom track errors. The standard deviation of the 20 repetitions of the vertical currents computations represents the uncertainty of the vertical currents. Most of the vertical currents had an uncertainty (σ_w) of one tenth of their value. If $\sigma_w \geqslant |w|$, the corresponding values are non-significant.

2.4.2. Nonlinear Ekman transport

Vertical currents created by winds near the front can be calculated with the following equations, the nonlinear Ekman transport (Eq. (9)) and its horizontal divergence (Eq. (10)):

$$\vec{E} = \frac{\vec{\tau} \times \vec{k}}{\rho(f + \zeta)} \tag{9}$$

$$w_E(0m) = -\vec{\nabla}.\vec{E} \tag{10}$$

where ζ is the relative vorticity calculated with ADCP data ($\zeta \sim \frac{-du}{dy}$ neglecting the $\frac{dv}{dx}$ component), which includes geostrophic and ageostrophic motions.

To test the nonlinear Ekman transport, wind velocity at 10 m above the surface and C_d, the drag coefficient, are used to calculate wind stress. The drag coefficient, also called a "friction coefficient", is the resistance that ocean waves exert on the atmosphere. It was calculated with a wave model as the ratio of the square of the friction velocity, to the square of the wind speed at a height of 10 m above the surface (ERA 5). Wind stress is calculated by the following equations:

$$\tau_x = \rho_{air}.C_d.|\vec{u}|.u_x, \tag{11}$$

$$\tau_y = \rho_{air}.C_d.|\vec{u}|.u_y. \tag{12}$$

Where u_x and u_y are the zonal and meridional components of the wind speed at 10 m above the sea surface, and $|\vec{u}|$ is its norm.

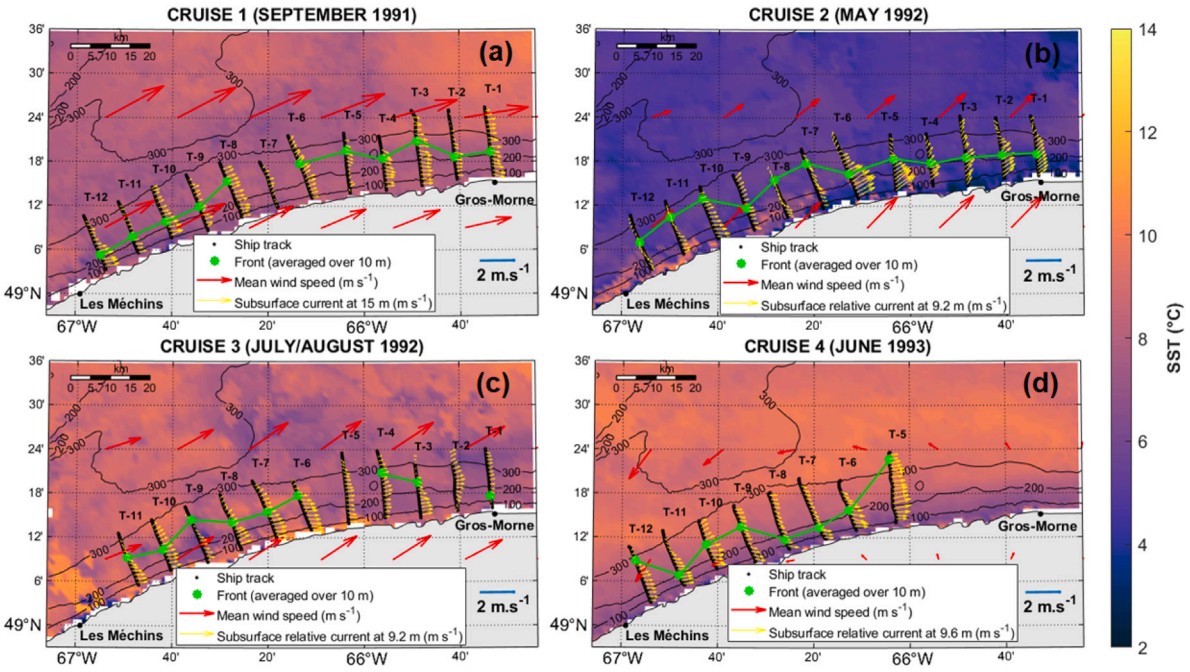

Fig. 7. Maps representing the front position for all cruises with SST (°C), average wind speed, and subsurface current (Cruise 1) or subsurface currents relative to the deepest measured currents (Cruises 2, 3, 4).

To obtain the boundary condition at the surface for the ω equation, we decompose the vertical velocities into an Ekman (w_E) and a geostrophic (w_g) components:

$$w(0m) = w_E(0m) + w_g(0m) = 0, \quad (13)$$

which yields the boundary condition for the geostrophic vertical velocity of the ω equation:

$$w_g(0m) = -w_E(0m) = \vec{\nabla}.\vec{E}. \quad (14)$$

Variations of w_g between the surface and 2 m are neglected because absolute geostrophic currents are calculated from 2 m below the surface (shallowest density data). The uncertainty of the resulting vertical currents is estimated in the same way as for the frontolysis and frontogenesis diagnosis.

3. Results

3.1. Variability of the Gaspé current front

Fig. 7 shows the front position along each transect of each cruise, overlaid on an SST satellite imagery averaged over a week during the period of each cruise. Near-surface ADCP currents and ERA 5 winds are also shown. The most notable result is that the front moves significantly from one cruise to the next. Its position cannot be predicted without in-situ data because it is a buoyancy-driven coastal jet with baroclinic instabilities leading to meandering (Sheng, 2001). Indeed, the general shape of the Gaspé Current front looks like a wavelike pattern due to the presence of meanders (Tang, 1980). The front position could not be detected for some transects due to the absence of a local density gradient maximum. Furthermore, the front position can vary over time scales ranging from a few hours to several days, as shown for Transect 10 of the first cruise which was repeated six times over two days (Fig. 8).

Fig. 7 also shows that the Gaspé current front is not characterized by a SST minimum. This is contrary to what has been reported by Tang's observations and model (Tang, 1982, 1983). Furthermore, the front retains a wavelike shape for all surveys.

Fig. 8 shows the short-term spatial and temporal variability of the Gaspé front. In 48 h, the maximum depth of the frontal isopycnal shallowed from 28 m to 6 m below the water surface and its horizontal position moved relative to the coast (Fig. 8a). The most pronounced shift occurred between the fourth and fifth repetition of the transect when the Gaspé Current and its front moved offshore (about 3.5 km in 18 h and 49 min), then moved inshore between the fifth and sixth repetition (about 2.5 km in 4 h and 17 min). These horizontal and vertical variabilities over a short period (48 h) characterize the unstable behavior of the Gaspé Current.

3.2. Detection of upwellings and downwellings

Water masses analyses were performed to detect occurrences of upwellings and downwellings near the Gaspé front. T-S diagrams of the different cruises showed the presence of four water masses (Fig. 9): (i) the estuary surface water (the least salty water mass) whose source is the St. Lawrence River upstream, (ii) the St. Lawrence Gulf surface water (the saltiest of the surface waters) which is composed of surface Atlantic waters coming from Belle-Isle and Cabot Straits, (iii) the intermediate cold water (the coldest water mass), which is created in winter and lies between the surface and the bottom water masses in spring and summer and (iv) the bottom water (the densest water mass) which is composed of deep Atlantic waters coming from Cabot Strait (Saucier et al., 2003).

For Cruise 4, there are obviously more than 3 reference water masses for the least-dense waters (Fig. 9d). Since we are restricted to 3 water masses for our analysis, we defined a hypothetical surface water mass for the estuary lying on the tangent to the mixing line between the intermediate cold water and the freshest surface waters observed in the T-S diagram at a temperature of 6 °C, corresponding to the sea surface temperature measured by satellite during the cruise (Fig. 7d). This hypothetical water mass encloses most of the CTD measurements in the resulting mixing triangle (Fig. 9d).

Mixing occurs between the surface waters of the estuary and Gulf of St. Lawrence and the intermediate cold water for all cruises (Fig. 9). After the water mass analysis of the 54 transects, Figs. 10 to 13 show examples of typical upwelling and downwelling situations near the

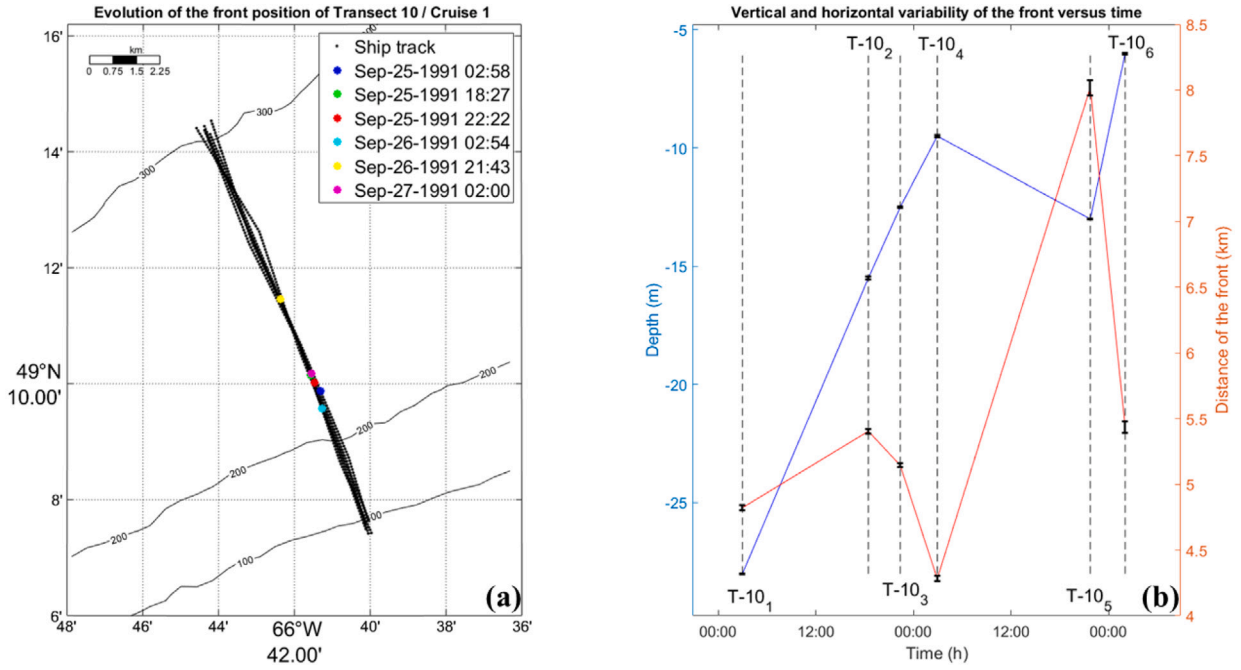

Fig. 8. Temporal variability of the front position and maximum depth of the frontal isopycnal during repetitions of CTD casts of transect 10/Cruise 1 (September 1991). Black vertical intervals show uncertainties (see Section 2.2).

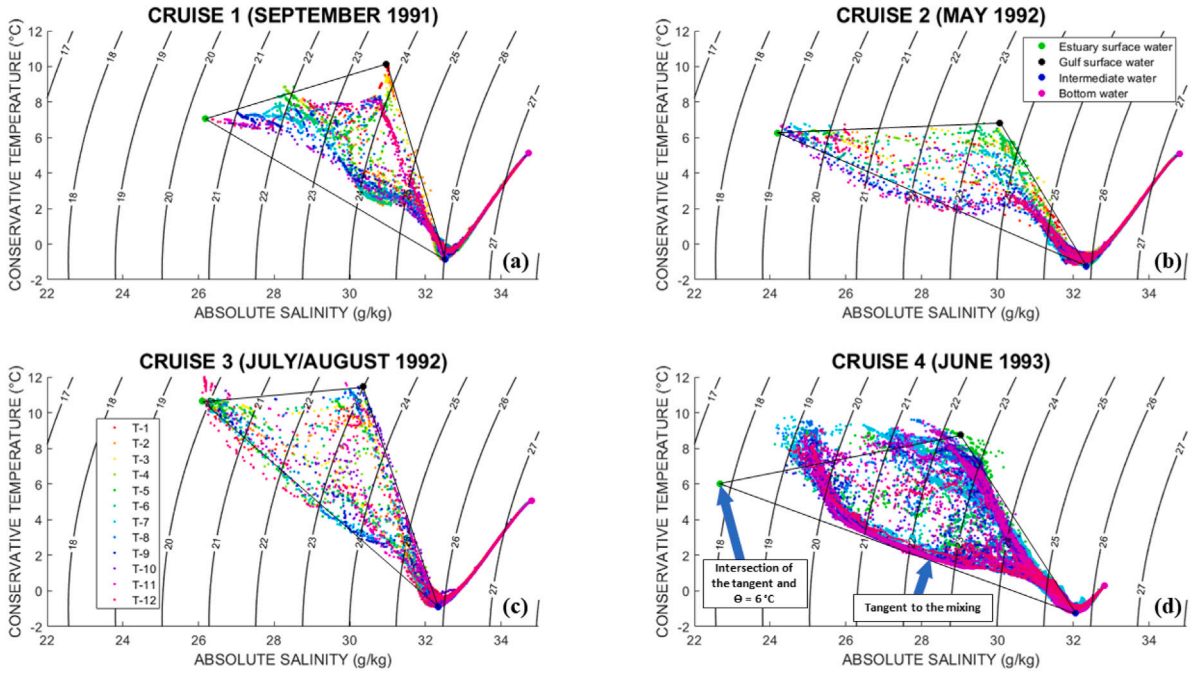

Fig. 9. T-S diagrams of all four cruises using the 12 transects of CTD casts (Cruises 1, 2, 3) and CTD-Vfin (Cruise 4) with the reference water masses.

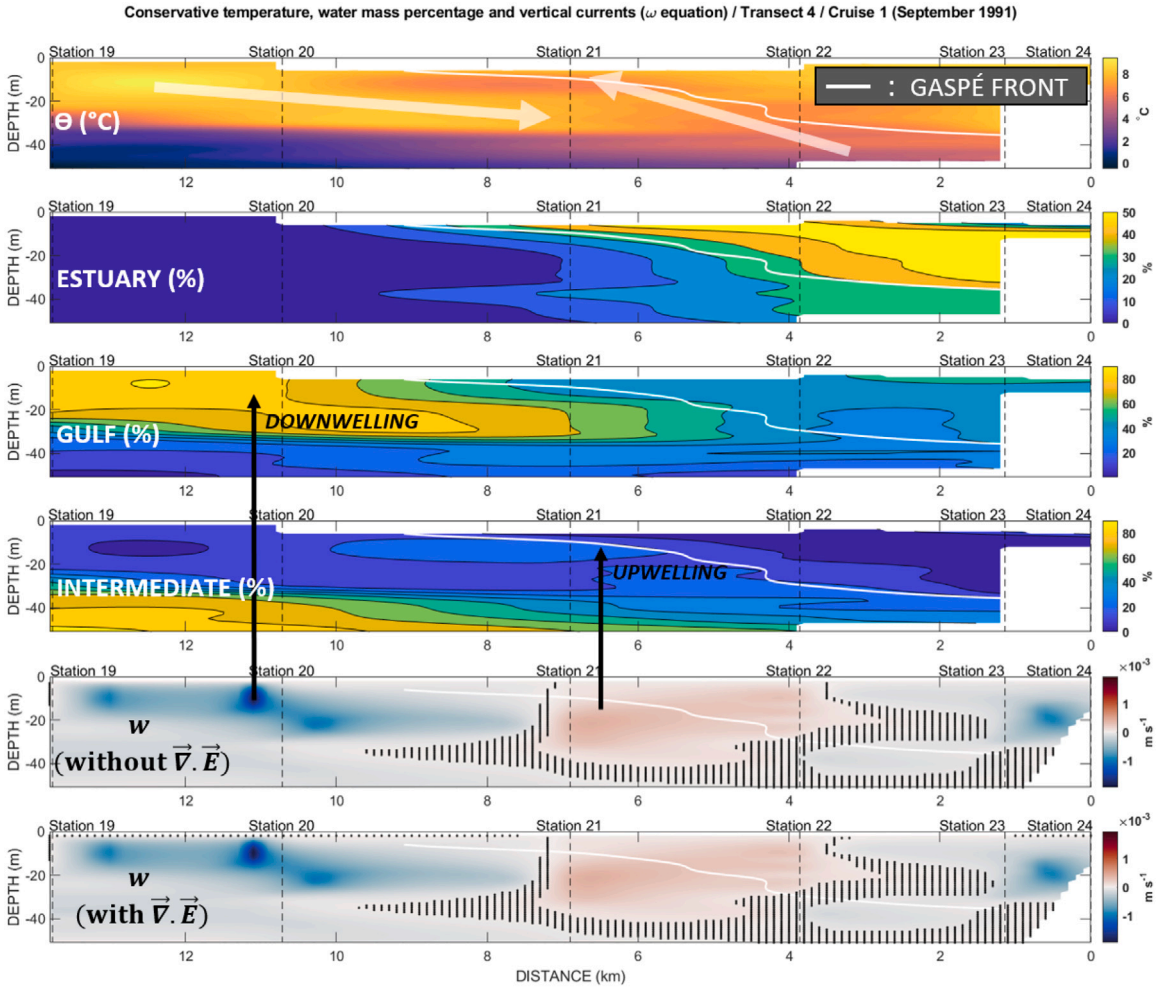

Fig. 10. Transects of conservative temperature, each water masses percentage and vertical currents (m s^{1}) calculated with the ω equation (without and with the Ekman surface boundary condition) for transect 4 of Cruise 1 (September 1991). Black hatchings represent the values where σ w $\geq$ |w|. Distance increases offshore from the station closest to shore.

Gaspé front. Transect 4 of Cruise 1 (Fig. 10) shows a downwelling of the relatively warm (9 °C) St. Lawrence Gulf's surface water offshore of the Gaspé front and an upwelling of the intermediate cold water just beneath the front, causing a surface temperature minimum (6 °C) at the edge of the front. This circulation pattern is opposite to that predicted by Tang (1982). Below the front (around 40 m depth), the estuary surface water is horizontally expelled offshore.

For transect 6 of Cruise 1 (Fig. 11), the distribution of water masses shows a downwelling of the surface estuary water occurring inside the Gaspé Current and an upwelling of the cold intermediate water crossing the front (around 20 m depth). Mixing between the three water masses takes place in the Gaspé Current explaining the high concentration (30%) of St. Lawrence Gulf's surface water. A downwelling of the St. Lawrence Gulf's surface water offshore the Gaspé Current is not observed in this example.

Configuration of water masses is more complex for transect 9 of Cruise 1 (Fig. 12). The distribution of water masses shows a downwelling of the St. Lawrence Gulf's surface water offshore the Gaspé Current front (local maximum horizontal density gradient) and under the offshore front (maximum horizontal density gradient). This downwelling occurs below 20 m depth. An upwelling of the intermediate water takes place under the Gaspé Current front. Another downwelling of the surface estuary water occurs inside the Gaspé Current.

An even more striking example similar to that shown for transect 4 of Cruise 1 (in Fig. 10) is shown for transect 4 of Cruise 4 (Fig. 13) from a CTD-VFIN transect with a better horizontal resolution. This time, however, a downwelling of the relatively warm (8 °C) St. Lawrence Gulf's surface water takes place just underneath the front and an upwelling of the intermediate cold (2 °C) water crosses the front, enters in the Gaspé Current and ascends to the surface just above the front, causing a surface temperature minimum (4 °C) on the shoreward edge of the front. This circulation pattern is again opposite to that predicted by Tang (1982, 1983).

For all transects of all cruises, we defined an upwelling event as the presence of a percentage of the cold intermediate water mass greater than or equal to 30% overlying waters with less that 30% of the cold intermediate water mass. Results are summarized in Table 1. The ω equation computations (with or without the nonlinear Ekman pumping) purpose is to confirm, or not, if these inferred upwellings and downwellings on the edge of the Gaspé Current result from the frontogenesis/frontolysis or nonlinear Ekman transport processes. Even if their presence is predominant (a percentage superior or equal to 71% of the total number of transects) for all four cruises, they are not a permanent feature over the entire length of the Gaspé Current front, and their positions relative to the front vary.

3.3. Generation mechanisms for upwellings and downwellings

3.3.1. Frontogenesis and frontolysis

Vertical currents obtained with the ω equation are shown for transects 4, 6 and 9 of Cruise 1 in Figs. 10, 11, and 12. Transect 4 of Cruise 1 (Fig. 10) shows an upwelling under the front and a downwelling

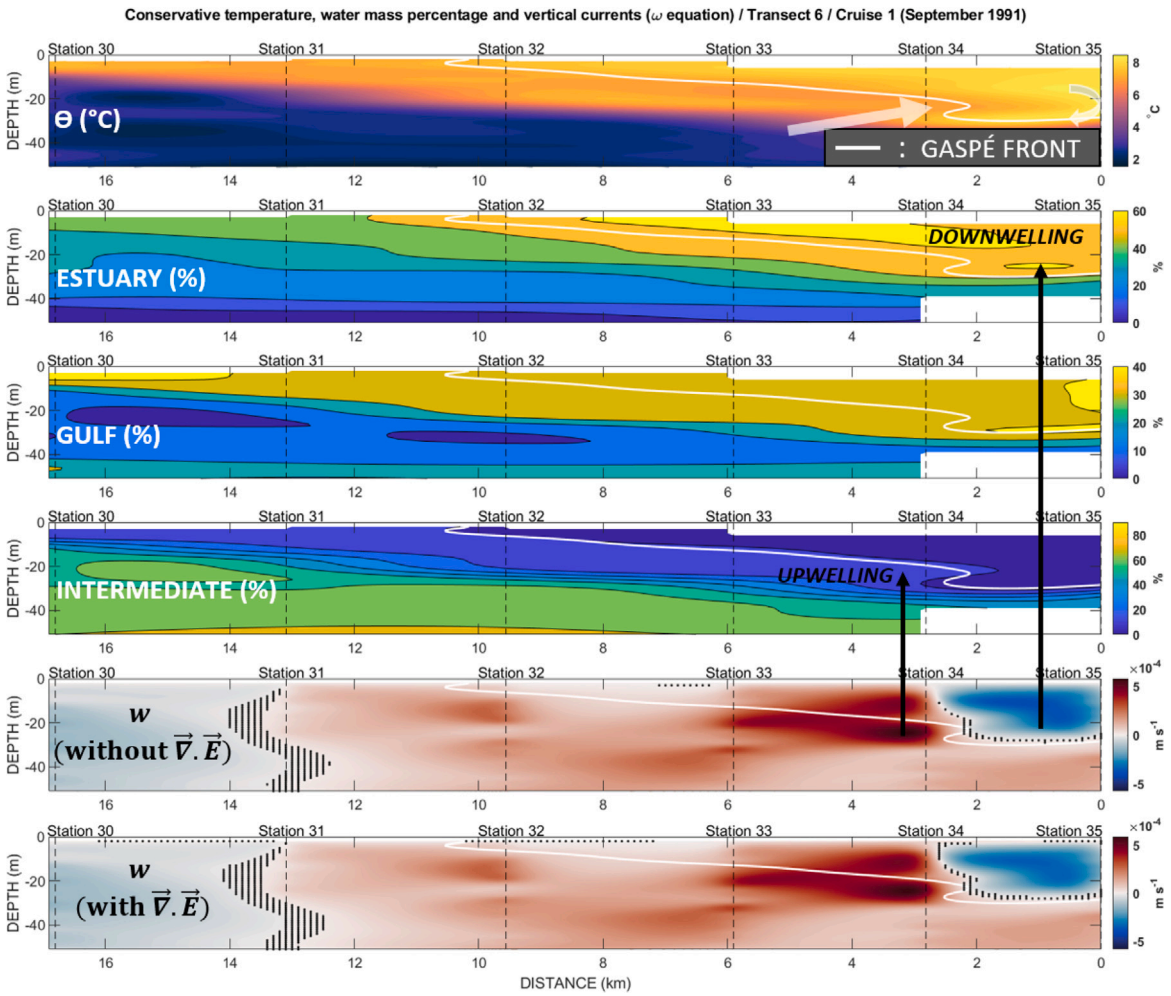

Fig. 11. Transects of conservative temperature, each water masses percentage and vertical currents (m s^{1}) calculated with the ω equation (without and with the Ekman surface boundary condition) for transect 6 of Cruise 1 (September 1991).

Table 1
Number of transects with upwelling for each cruise.

Cruises	Number of transects (A)	With upwelling near the front (B)	Ratio (B/A)
Cruise 1 – CTD (September 1991)	17	12	0.71
Cruise 2 – CTD (May 1992)	12	9	0.75
Cruise 3 – CTD (July/August 1992)	11	9	0.82
Cruise 4 – CTD Vfin (June 1993)	14	13	0.93
All cruises	54	43	0.8

offshore of the front via the water masses analysis, which matches well with the vertical currents diagnosed by the ω equation. This suggests that these inferred upwelling and downwelling are caused by frontogenesis (strengthening of the front). Transect 6 (Fig. 11) of Cruise 1 is particularly interesting as it displays the presence of a strong downwelling of the estuary surface waters occurring inside the Gaspé Current with a velocity approaching -3.10^{-4} m s^{-1} (the minimum value of the transect) and an upwelling of the intermediate cold water occurring under the front crossing it with a velocity approaching 6.10^{-4} m s^{-1} (the maximum value of the transect). This phenomenon is visible in the intermediate water mass percentage, with an overturn occurring where the upwelling crosses the front. This is the manifestation of a frontolysis case (weakening of the front). Transect 9 (Fig. 12) of Cruise 1 is more complex showing two fronts. One local front corresponds to the Gaspé Current front (a local maximum of density gradient) and one offshore front (corresponding to the maximum value of the density gradient which is positioned the most offshore). The transect displays the presence of two downwellings: one with the Gulf surface waters occurring under the offshore front with a vertical velocity approaching -1.10^{-4}m s^{-1} and another one occurring inside the Gaspé Current with the estuary surface waters and a vertical velocity approaching -1.5×10^{-4} m s^{-1}. An upwelling of the intermediate waters occurs below the Gaspé front with a velocity approaching 0.5×10^{-4} m s^{-1}. As for transect 6, this is the manifestation of a frontolysis case. Overall, frontogenesis and frontolysis diagnosed with the ω equation match with upwellings and downwellings inferred from the water masses analysis near the Gaspé Current front for all transects of Cruise 1 except for transect 2, without counting the first and last transects and the repetitions of transect 10 as frontolysis and frontogenesis cannot be tested in these cases (see Section 2.4). Fig. 14 shows vertical currents diagnosed from the ω equation and isopycnals interpolated over the entire area of Cruise 1 at 10 m depth, with a typical example of frontogenesis along the transect 4, where the isopycnals are contracting (frontogenesis), with vertical circulation tending to counteract frontogenesis. However, not all cases of frontolysis and frontogenesis during Cruise 1 can be seen as they occur at varying depths.

3.3.2. Nonlinear Ekman transport

Vertical currents calculated with the ω equation, and the surface boundary conditions associated with the nonlinear Ekman transport

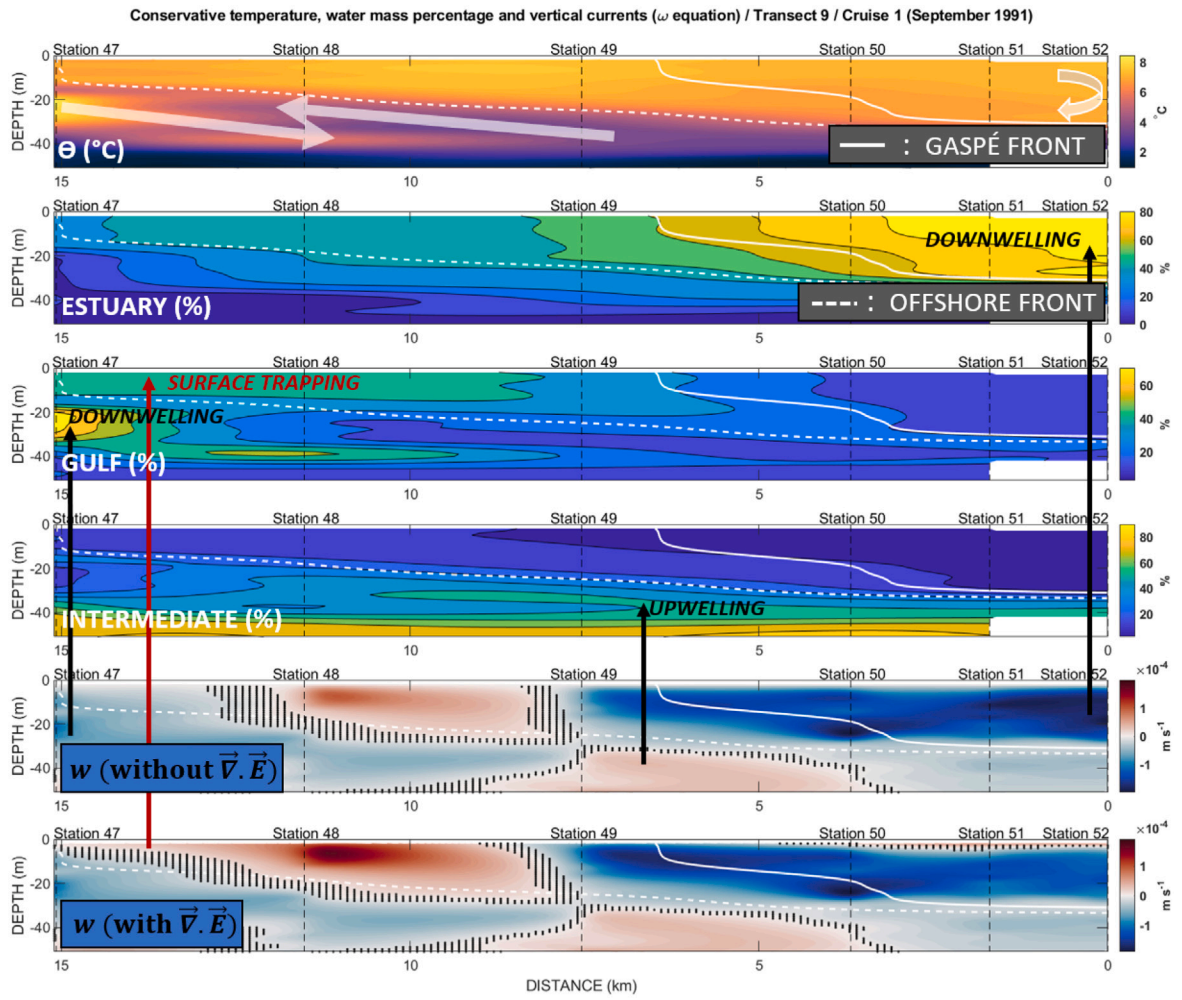

Fig. 12. Transects of conservative temperature, each water masses percentage and vertical currents (m s^{1}) calculated with the ω equation (without and with the Ekman surface boundary condition) for transect 9 of Cruise 1 (September 1991).

(Eq. (14)) are also shown in Figs. 10, 11, and 12. For transects 4 and 6 of Cruise 1 (Figs. 10 and 11), the effect of nonlinear Ekman transport is negligible compared to the frontolysis and frontogenesis mechanism since the southerly winds (Fig. 15) do not affect the formation of upwellings and downwellings near the front. However, the nonlinear Ekman pumping can become significant near the surface (Fig. 12) when westerly or easterly winds occur like during transect 9 of Cruise 1 when winds were westerly (Fig. 15). A surface trapping (created by winds) is formed near the surface (first 10 m offshore of the Gaspé Current front) and affects the water column's composition. A part of the Gulf water mass downwelled offshore is retained at the surface near the edge of the offshore front, which explains the observed high percentage (40%). Without the divergence of the nonlinear Ekman transport, a downwelling would be diagnosed from the ω equation. Overall, for all transects of Cruise 1, winds cannot explain upwellings and downwellings formation at the depth of the cold intermediate water mass.

4. Discussion

Tang (1982) proposed an analytical model of frontal upwelling to explain the generation mechanism of upwellings and downwellings observed near the Gaspé Current front. This model postulated the existence of an interfacial Ekman transport beneath the front, causing a permanent downwelling of offshore surface waters below the front, and a permanent upwelling of intermediate waters further offshore to close the cross-frontal circulation. The water masses analysis of in-situ observations of temperature and salinity across the front do not support the predictions of Tang (1982). Upwellings and downwellings are not permanent features and upwellings are not always located offshore of the front. In fact, the circulation pattern most typically observed is in the opposite direction to that predicted by Tang (1982)'s model. Our results are in line with previous observations showing that the temperature minimum near the surface appears inside the Gaspé Current (Levasseur et al., 1992).

Considering the discrepancies between the model proposed by Tang (1982), summed up as a permanent upwelling offshore and a permanent downwelling under the Gaspé Current front, and observations, we investigated whether upwellings and downwellings could be caused by more classical mechanisms such as nonlinear Ekman pumping (Stern, 1965) and frontogenesis/frontolysis (Hoskins and Bretherton, 1972).

The frontogenesis/frontolysis hypothesis (Fig. 16) appears to be at work for 87.5% corresponding to seven out of eight transects of Cruise 1 presenting an upwelling or a downwelling without counting the first and last transects as well as repetitions of transect 10 (see Section 2.4). For the other 12.5%, three hypotheses can be made: (i) another mechanism generates upwellings and downwellings, (ii) the trace of a high percentage of the intermediate water near the front may be the manifestation of an ancient upwelling, or (iii) interpolation of three consecutive transects not sampled closely enough in time and space leads to biased results due to the fast-evolving Gaspé Current dynamics. Indeed, repetitions of transect 10 of Cruise 1 showed that short events

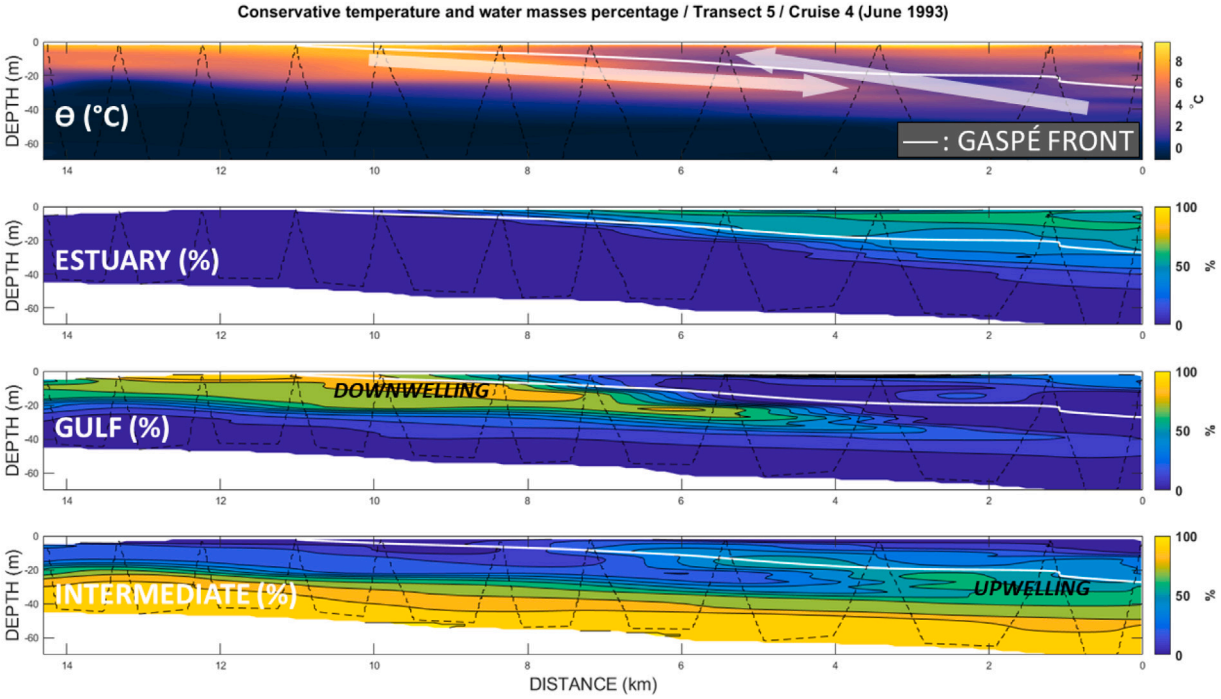

Fig. 13. Temperature transects and each water masses percentage for transect 5 of Cruise 4 (June 1993).

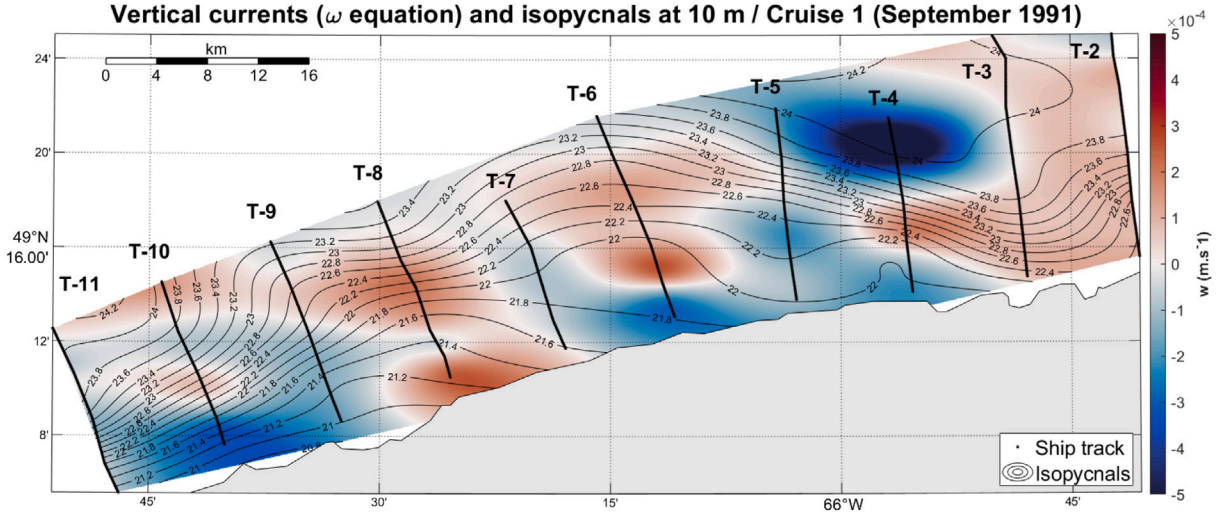

Fig. 14. Vertical currents diagnosed from the ω equation and isopycnals interpolated over the whole area of Cruise 1 at 10 m depth.

can occur and move the front relative to the coast. Furthermore, frontal instabilities of the Gaspé current typically have wavelengths of 40 to 60 km (Mertz et al., 1988; Mertz and El-sabh, 1989), hence the ~10 km spacing between our transects should resolve them.

Concerning Ekman pumping, the results showed that nonlinear Ekman transport is not the key mechanism that causes deep upwellings of the intermediate waters and deep downwellings of the Gulf of St. Lawrence surface waters near the front during September 1991. However, the low resolution of winds data (0.25° × 0.25° grid) may underestimate winds stress curl caused by small scale variations of winds, hence underestimating the contribution of nonlinear Ekman transport to vertical motions. Another possible effect could be the wind modulation by SST gradient. Using the relation between wind stress curl and SST gradients found by Chelton et al. (2001), their Figs. 10 and 11, we estimated that for a SST gradient of 5 degrees Celsius over 20 km (Fig. 7d), the vertical velocities caused by this SST-induced winds stress curl would be of about $2.5.10^{-5}$ m s^{-1}, which is one order of magnitude smaller than the velocities diagnosed by the omega equation (Figs. 10 to 14). Nevertheless, with these data, results showed that for shallow waters, upwellings and downwellings could be the result of along front winds (e.g. Fig. 12). Moreover, winds could have an indirect effect on vertical motions caused by frontogenesis and frontolysis, since wind pulses could help trigger instabilities of the Gaspé Current (Mertz et al., 1988).

According to Benoit et al. (1985), considering the seasonal cycle, an increase in salinity occurs from the end of June to November in the current due to the decrease of less saline waters flow from the estuary. Being controlled by this salinity front (Benoit et al., 1985), the estuary flow variation thus affects the Gaspé Current dynamics. A strong flow in May and June with a peak of 0.03 Sv (Koutitonsky and Bugden, 1991)

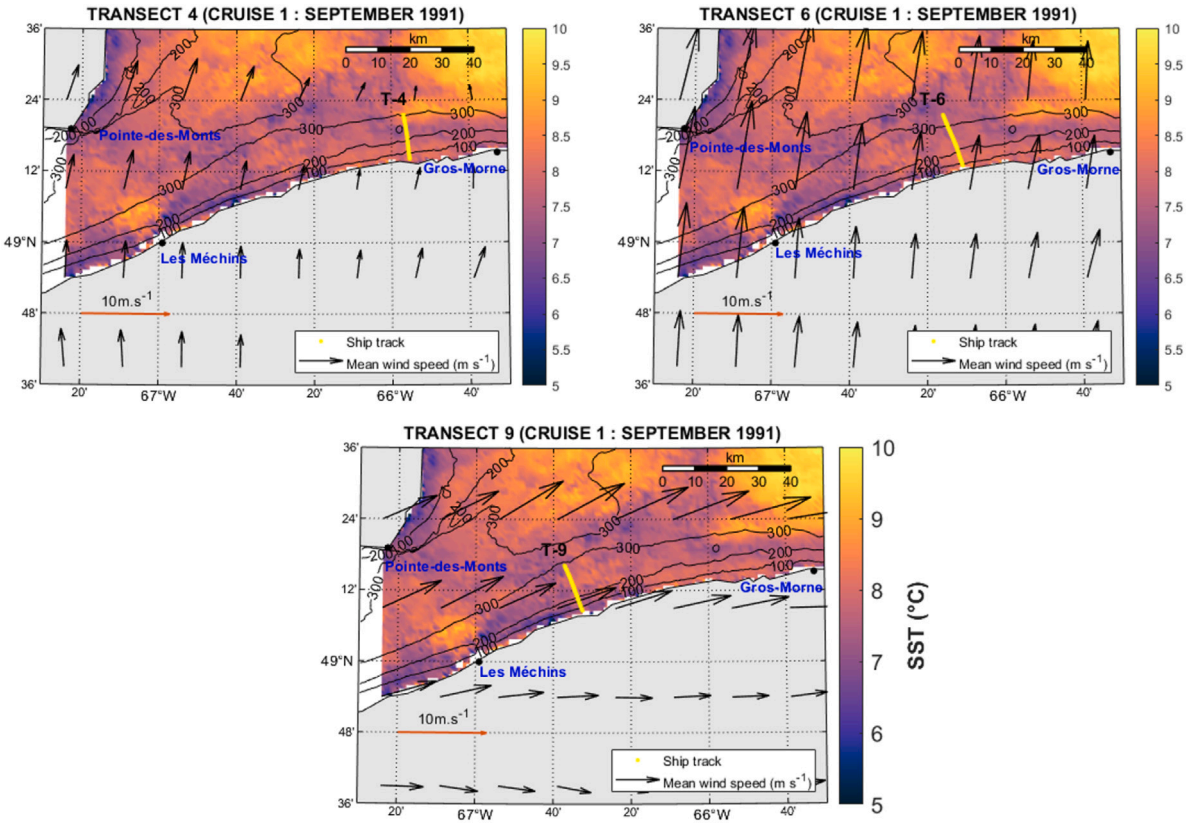

Fig. 15. Winds (black arrows) during the transects 4, 6 and 9 of Cruise 1 with cruise-averaged SST (°C) in September 1991.

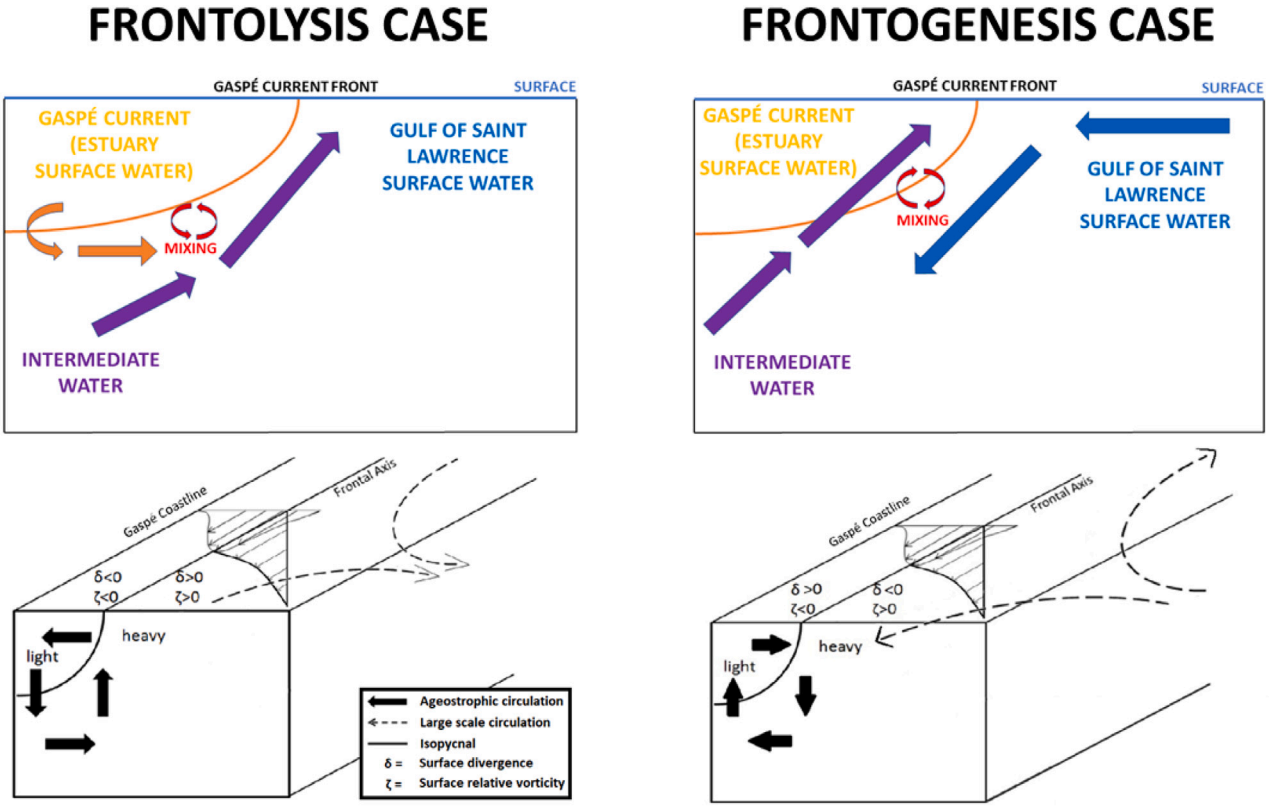

Fig. 16. Schematic of frontolysis (left) and frontogenesis (right) leading to the creation of upwellings and downwellings on the edge of the Gaspé Current. Bottom schematics are modified from McWilliams et al. (2009) adapted to the Gaspé Current area.

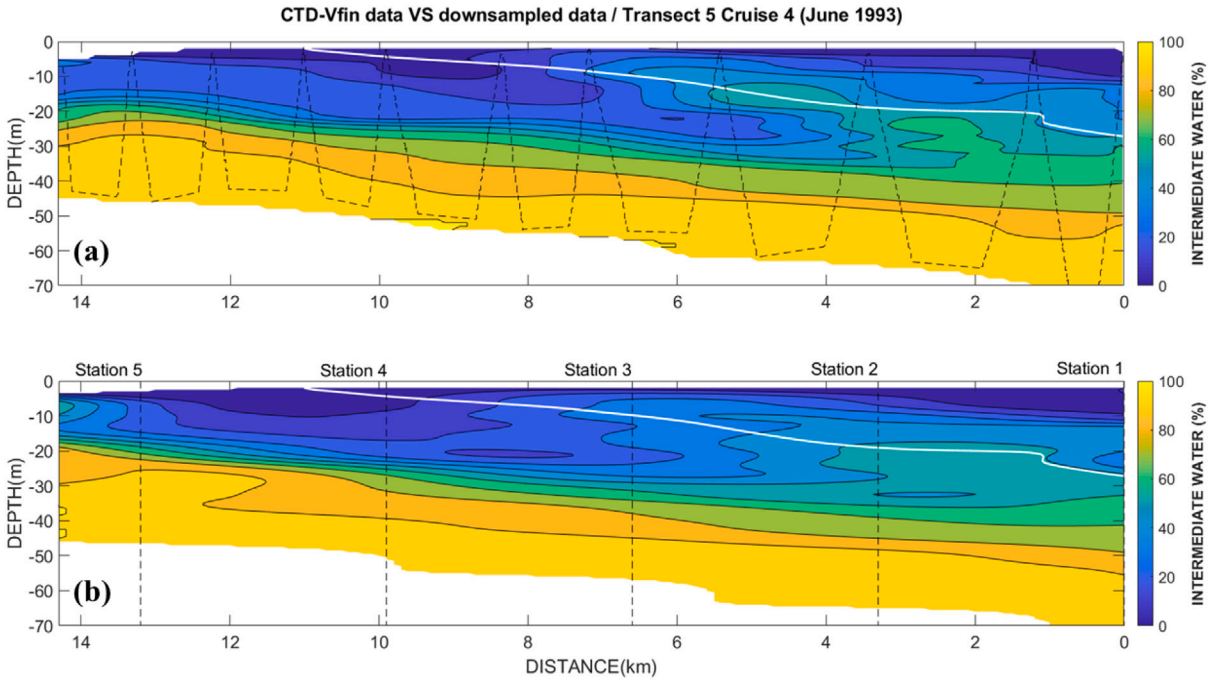

Fig. 17. (a) Example of a CTD V-FIN intermediate water percentage transect versus (b) downsampled data (Transect 5, Cruise 4).

will increase the vertical shears and could be favorable to the formation of baroclinic instabilities (Mertz et al., 1988; Sheng, 2001), leading to the variation of the Gaspé Current general shape as shown in Fig. 7. However, even if the flow's intensity starts decreasing at the end of June, the results also showed that in September 1991 and July/August 1992, the front retains a wavelike shape. Mertz et al. (1988) have also observed meanders even when the estuary runoff is only 60% of its maximum spring value.

We have not considered the effect of bottom topography on vertical motion, because the position of meanders from one cruise to another radically changed (Fig. 7), and therefore are not associated with bathymetric features. Vertical motions diagnosed by the ω equation are consistent with our water masses analysis, suggesting that vertical motions are mostly generated by frontogenesis and frontolysis rather than topographic accidents. Moreover the Gaspé Current is mostly parallel to the coastline, and confined in the top 50 m well above the seafloor at the location of the front, which ranges between 150 m and 300 m.

In conclusion, when the Gaspé Current meanders, strain-induced frontogenesis and frontolysis of the Gaspé Current front will generate upwellings and downwellings near the front, a phenomenon which has been shown to be at play at many other fronts in the ocean, such as the Azores front (Rudnick, 1996), the Mississippi plume front (Kobashi and Hetland, 2020), the Gulf Stream (Thomas and Joyce, 2010a), and the subpolar front of the Japan/East Sea (Thomas et al., 2010b), among others. Vertical motions at fronts may also be caused by other mechanisms, such as non-linear Ekman pumping (Niiler, 1969) or near-inertial oscillations (Thomas et al., 2010b). For the Gaspé Current front, our results suggest that non-linear Ekman pumping may generate significant vertical motions near the surface, but strain-induced frontogenesis and frontolysis remains the dominant mechanism for deeper motions reaching the nutrient-rich cold intermediate layer. We have not investigated the effect of time-dependent processes such as inertial or superinertial motions, despite the observed variability of the front on short time scales (Fig. 8), due to the limited spatio-temporal sampling of the front. Taking into account the effect of time-dependent processes will require new observational campaigns with higher spatio-temporal resolution.

CRediT authorship contribution statement

Théau Leclercq: Writing – original draft, Software, Formal analysis. **Cédric Chavanne:** Writing – review & editing, Supervision, Methodology, Funding acquisition. **Pierre Larouche:** Writing – review & editing, Supervision, Funding acquisition, Conceptualization.

Declaration of competing interest

The authors declare that they have no known competing financial interests or personal relationships that could have appeared to influence the work reported in this paper.

Data availability

This unique set of CTD casts, CTD V-FIN, and ADCP data acquired by Pierre Larouche, third author of this manuscript, between 1991 and 1993 on the edge of the Gaspé Current has been submitted and published to the SLGO (St. Lawrence Global Observatory) data management office to create a publicly accessible ERDDAP database and generate a DOI.

The DOI of this data set is https://doi.org/10.26071/ogsl-9acdc006-20cb, its URL is https://catalogue.preprod.ogsl.ca/dataset/ca-cioos_9acdc006-20cb-4c7e-8aae-ca1007cf9b63 and the citation is Larouche (2023).

SST data and their technical report are publicly available at SLGO:
https://ogsl.ca/en/satellite-remote-sensing-data-information/
https://ogsl.ca/en/satellite-remote-sensing-application/

CTD V-FIN Data are available via this SLGO link:
Click here to access CTD V-FIN data.

Wind reanalysis data are publicly available with the ERA5 model however you need to subscribe to have them:
https://cds.climate.copernicus.eu/cdsapp#!/dataset/reanalysis-era5-single-levels?tab=overview.

Acknowledgments

Financial support to T. Leclercq was provided by NSERC, Canada (Grant RGPIN-2018-06585 to Chavanne), ISMER, Canada, and Québec-Océan, Canada. The in-situ data collection was funded by the MPO and the Canadian Space Agency.

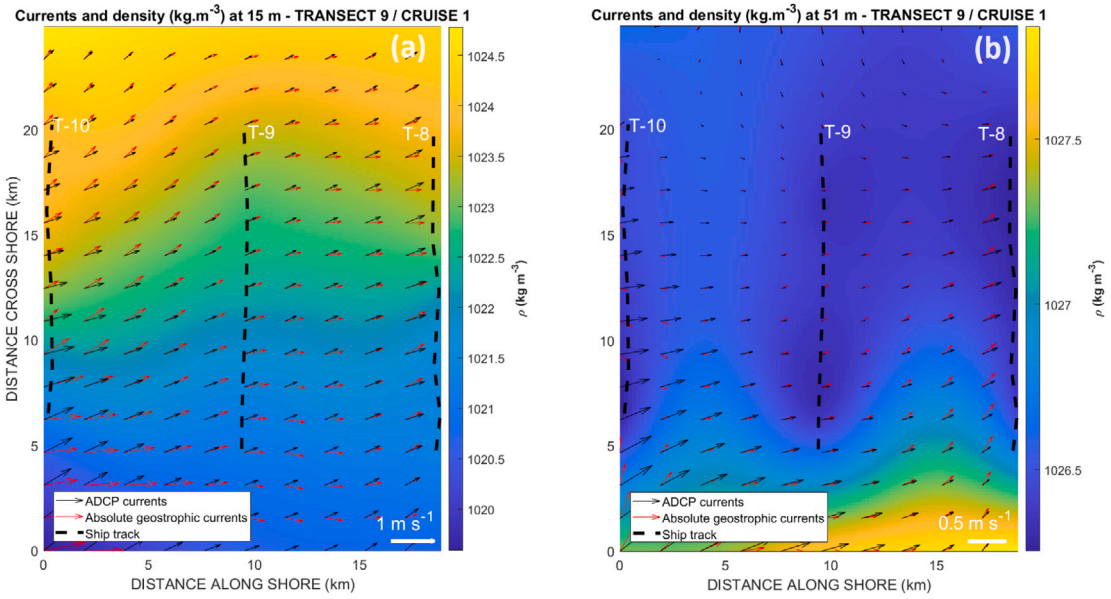

Fig. 18. ADCP data (black arrows) vs absolute geostrophic currents (red arrows) on a horizontal plane with interpolated density at (a) 15 m and (b) 51 m depth. (For interpretation of the references to color in this figure legend, the reader is referred to the web version of this article.)

Appendix A

A.1. Test of CTD casts horizontal resolution

During Cruise 4 in June 1993, a CTD V-FIN was towed behind the ship, profiling the water column in a V-shape pattern, and providing a much higher horizontal resolution than that obtained with the standard CTD casts of the other cruises. An example of the percentage of intermediate water is shown in Fig. 17a revealing, in particular, some upwelling across the front within the first 8 kms of the transect. To verify whether this upwelling would have been observed using the lower spatial resolution CTD casts of the previous cruises, synthetic CTD data having the average separation distance of the casts of the three other cruises were calculated by interpolating the high-resolution optimally interpolated CTD data from the V-FIN. The synthetic CTD casts were then used to determine the percentage of the reference water masses, which were then optimally interpolated (Fig. 17b). Although some small-scale features are missing, the upwelling in the first 8 kms of the transect is still observed, confirming that the lower spatial resolution of the CTD casts sampling of the first three cruises can resolve the prominent horizontal and vertical processes within the Gaspé Current.

A.2. Geostrophic versus ADCP currents

Absolute geostrophic currents (Figs. 18a, b, 19b) are calculated using (Rudnick, 1996) method by using a stream function ψ (x,y) and interpolated density and horizontal currents for each depth on a 2D grid (horizontal plane). They are shown on a horizontal (Fig. 18) and vertical plane (Fig. 19). Absolute geostrophic currents are compared to ADCP currents (Figs. 18a, b, 19a). As expected, the fronts correspond to the near-surface maximum values of the along-shore geostrophic currents (Fig. 19b).

A.3. Test of boundary conditions for the ω equation

Vertical currents diagnosed with the ω equation are obtained using (20a) Dirichlet or (20b) Neumann boundary conditions for transect 9 of Cruise 1. Their differences are shown in panel c. The root mean square of the differences is less than 2% of the root mean square of w.

Appendix B. Open research

B.1. Data availability statement (CTD, CTD V-FIN, ADCP, SST, and ERA5 data)

This set of CTD casts, CTD V-FIN, and ADCP data acquired by Pierre Larouche between 1991 and 1993 has been made publicly available on the SLGO (St. Lawrence Global Observatory) portal at https://catalogue.preprod.ogsl.ca/dataset/ca-cioos_9acdc006-20cb-4c7e-8aae-ca1007cf9b63 and the citation is Larouche (2023).

SST data and their technical report are publicly available at SLGO: https://ogsl.ca/en/satellite-remote-sensing-data-information/ https://ogsl.ca/en/satellite-remote-sensing-application/

Wind reanalysis data are publicly available at this link (requires registration to access the data): https://cds.climate.copernicus.eu/cdsapp#!/dataset/reanalysis-era5-single-levels?tab=overview

B.2. Software availability statement

Raw CTD cast data were processed using standard quality control procedures (Sea-Bird Scientific, 2017) by the data management section of the Maurice-Lamontagne Institute.

Raw CTD V-FIN data were also processed using the same quality standard procedures by Leclercq T., first author, including pressure loops correction.

Conservative temperature, absolute salinity, and seawater density were computed using the TEOS-10 algorithms (https://www.teos-10.org/pubs/gsw/html/gsw_contents.html) on R2019 MatLab version. Procedures can be found following this reference (McDougall, T. J., and Barker, P. M. (2011). Getting started with TEOS-10 and the Gibbs Seawater (GSW) oceanographic toolbox. SCOR/IAPSO Working Group, 127, 1-28.).

3D interpolation with smoothness parameter was processed using Nicholson, J. (2021) algorithms. (Nicholson, J. (2021), "regularizeNd" MATLAB Central File Exchange, version 2.4.0, available from https://www.mathworks.com/matlabcentral/fileexchange/61436-regularizend).

Maps were created with M_Map package following this reference: Pawlowicz, R., (2020), M_Map: A mapping package for MATLAB. version 1.4 m, [Computer software], available online at www.eoas.ubc.ca/~rich/map.html.

All other analyses and processing was performed on R2019a MatLab version by Leclercq, T. (first author).

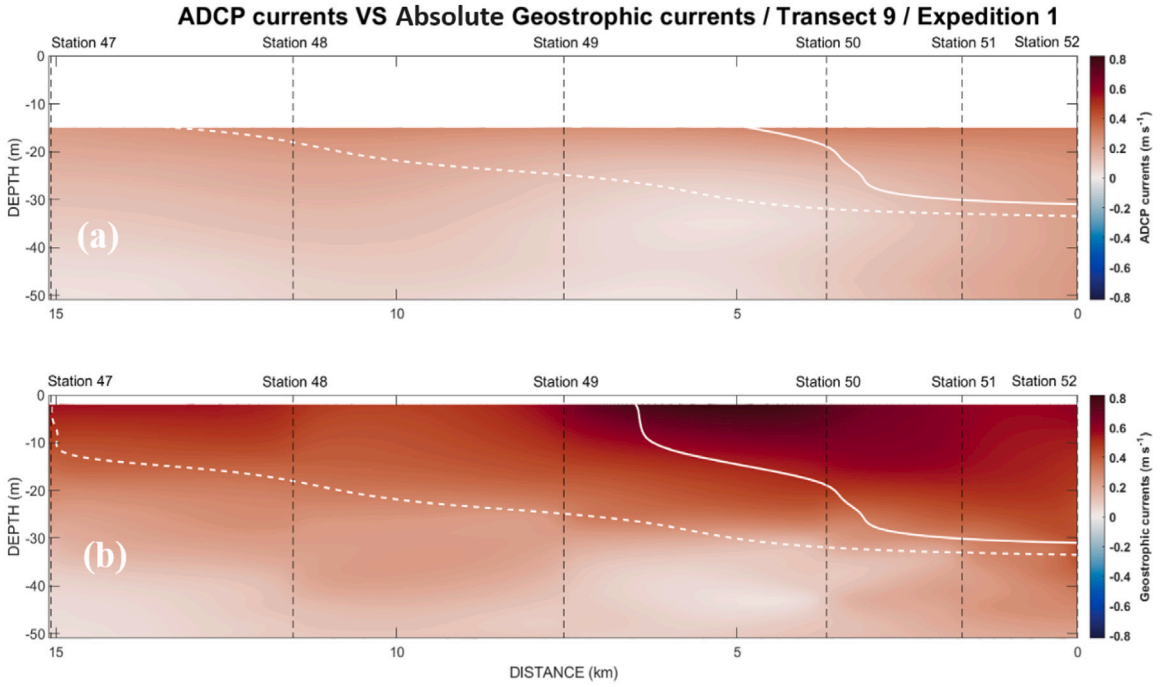

Fig. 19. (a) ADCP vs (b) absolute geostrophic along-shore currents on a vertical plane for Transect 9 of Cruise 1 (September 1991). The dashed white line represents the offshore front, and the white line represents the Gaspé Current front.

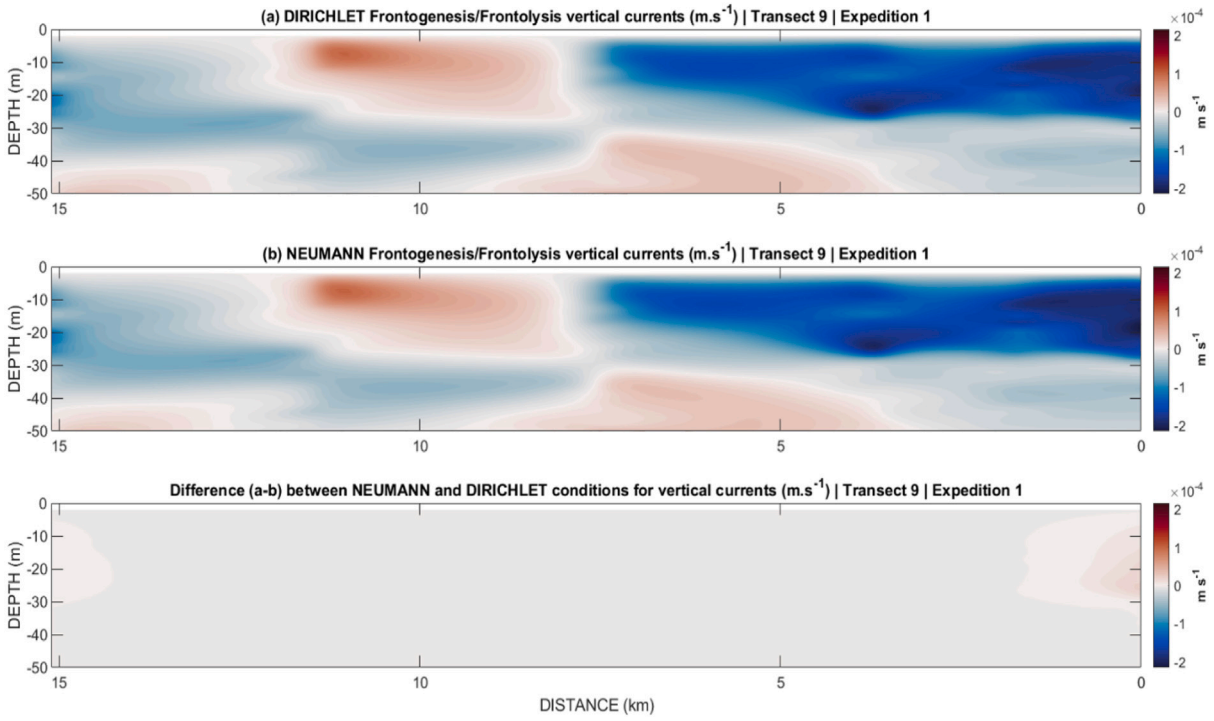

Fig. 20. Vertical currents calculated with (a) Dirichlet boundary conditions, (b) Neumann boundary conditions and (c) their differences.

References

Mertz, G., Koutitonsky, V.G., Gratton, Y., El-Sabh, M.I., 1992. Wind-induced eddy motion in the lower St. Lawrence estuary. Estuar. Coast. Shelf Sci. 34 (6), 543–556. http://dx.doi.org/10.1016/S0272-7714(05)80061-7.

Sheng, J., 2001. Dynamics of a buoyancy-driven coastal jet: The gaspé current. J. Phys. Oceanogr. 31 (11), 3146–3162. http://dx.doi.org/10.1175/1520-0485(2001)031<3146:DOABDC>2.0.CO;2.

Benoit, J., El-Sabh, M.I., Tang, C.L., 1985. Structure and seasonal characteristics of the gaspé current. J. Geophys. Res.: Oceans 90 (C2), 3225–3236. http://dx.doi.org/10.1029/JC090iC02p03225.

Farquharson, W., 1962. Tides, tidal streams and currents in the Gulf of St. Lawrence. Canadian Hydrographic Service, Marine Sciences Branch, Department of Mines and Technical Surveys, Ottawa, Canada, pp. 61–62.

Mertz, G., El-Sabh, M.I., Proulx, D., Condal, A.R., 1988. Instability of a buoyancy-driven coastal jet: The gaspé current and its St. Lawrence precursor. J. Geophys. Res.: Oceans 93 (C6), 6885–6893. http://dx.doi.org/10.1029/JC093iC06p06885.

Hoskins, B.J., Bretherton, F.P., 1972. Atmospheric frontogenesis models: Mathematical formulation and solution. J. Atmos. Sci. 29 (1), 11–37. http://dx.doi.org/10.1175/1520-0469(1972)029<0011:AFMMFA>2.0.CO;2.

McWilliams, J.C., Colas, F., Molemaker, M.J., 2009. Cold filamentary intensification and oceanic surface convergence lines. Geophys. Res. Lett. 36 (18), http://dx.doi.org/10.1029/2009GL039402.

Tang, C.L., 1982. A model for frontal upwelling. In: Nihoul, J.C. (Ed.), Hydrodynamics of Semi-Enclosed Seas. In: Elsevier Oceanography Series, vol. 34, Elsevier, pp. 329–348. http://dx.doi.org/10.1016/S0422-9894(08)71249-2.

Tang, C.L., 1983. Cross-front mixing and frontal upwelling in a controlled quasi-permanent density front in the gulf of St. Lawrence. J. Phys. Oceanogr. 13 (8), 1468–1481. http://dx.doi.org/10.1175/1520-0485(1983)013<1468:CFMAFU>2.0.CO;2.

Stern, M.E., 1965. Interaction of a uniform wind stress with a geostrophic vortex. Deep Sea Res. Oceanogr. Abstr. 12 (3), 355–367. http://dx.doi.org/10.1016/0011-7471(65)90007-0.

Niiler, P.P., 1969. On the ekman divergence in an oceanic jet. J. Geophys. Res. 74 (28), 7048–7052. http://dx.doi.org/10.1029/JC074i028p07048.

Larouche, P., 1993a. Profils de salinité et de température recueillis dans le courant de gaspé. Volume 1: Septembre 1991. Rapport Stat. Can. Sur L'hydrogr. Les Sci. Océan. 119, v+119.

Larouche, P., 1993b. Profils de salinité et de température recueillis dans le courant de gaspé. Volume 2: Mai 1992. Rapport Stat. Can. Sur L'hydrogr. Les Sci. Océan. 119, v+134.

Larouche, P., 1993c. Profils de salinité et de température recueillis dans le courant de gaspé. Volume 3: Août 1992. Rapport Stat. Can. Sur L'hydrogr. Les Sci. Océan. 119, v+96.

Larouche, P., 1993d. Profils de salinité et de température recueillis dans le courant de gaspé. Volume 4: Juin 1993. Rapport Stat. Can. Sur L'hydrogr. Les Sci. Océan. 119, v+46.

Larouche, P., 2023. Oceanographic Campaigns in the Gaspé Current (September 1991, May 1992, August 1992 and June 1993) [Data set]. St. Lawrence Global Observatory (SLGO), http://dx.doi.org/10.26071/ogsl-9acdc006-20cb, https://catalogue.preprod.ogsl.ca/dataset/ca-cioos_9acdc006-20cb-4c7e-8aae-ca1007cf9b63.

Larouche, P., 1996. Observation of the gaspé current using ERS-1 SAR. Can. J. Remote Sens. 22 (4), 420–427. http://dx.doi.org/10.1080/07038992.1996.10874665.

Sea-Bird, 2017. Software Manual Seasoft V2: SBE Data Processing. Sea-Bird Scientific: Bellevue, WA, USA, p. 177.

McDougall, T.J., Barker, P.M., 2011. Getting started with TEOS-10 and the gibbs seawater (GSW) oceanographic toolbox. Scor/Iapso Work. Group 127 (532), 1–28.

Adrados, C., Girard, I., Gendner, J.-P., Janeau, G., 2002. Global positioning system (GPS) location accuracy improvement due to selective availability removal. Comptes Rendus Biol. 325 (2), 165–170. http://dx.doi.org/10.1016/S1631-0691(02)01414-2.

Bretherton, F.P., Davis, R.E., Fandry, C., 1976. A technique for objective analysis and design of oceanographic experiments applied to MODE-73. Deep Sea Res. Oceanogr. Abstr. 23 (7), 559–582. http://dx.doi.org/10.1016/0011-7471(76)90001-2.

Chelton, D.B., DeSzoeke, R.A., Schlax, M.G., El Naggar, K., Siwertz, N., 1998. Geographical variability of the first baroclinic rossby radius of deformation. J. Phys. Oceanogr. 28 (3), 433–460. http://dx.doi.org/10.1175/1520-0485(1998)028<0433:GVOTFB>2.0.CO;2.

Thomson, R.E., Emery, W.J., 2014. Data analysis methods in physical oceanography, third ed. Elsevier, Amsterdam, pp. 226–288.

Gasparin, F., Maes, C., Sudre, J., Garcon, V., Ganachaud, A., 2014. Water mass analysis of the coral sea through an optimum multiparameter method. J. Geophys. Res.: Oceans 119 (10), 7229–7244. http://dx.doi.org/10.1002/2014JC010246.

Hoskins, B.J., Draghici, I., Davies, H.C., 1978. A new look at the ω-equation. Q. J. R. Meteorol. Soc. 104 (439), 31–38. http://dx.doi.org/10.1002/qj.49710443903.

Pinot, J.-M., Tintoré, J., Wang, D.-P., 1996. A study of the omega equation for diagnosing vertical motions at ocean fronts. J. Mar. Res. 54 (2), 239–259. http://dx.doi.org/10.1357/0022240963213358.

Viúdez, Á., Tintoré, J., Haney, R.L., 1996. About the nature of the generalized omega equation. J. Atmos. Sci. 53 (5), 787–795. http://dx.doi.org/10.1175/1520-0469(1996)053<0787:ATNOTG>2.0.CO;2.

Giordani, H., Prieur, L., Caniaux, G., 2006. Advanced insights into sources of vertical velocity in the ocean. Ocean Dyn. 56, 513–524. http://dx.doi.org/10.1007/s10236-005-0050-1.

Rudnick, D.L., 1996. Intensive surveys of the azores front: 2. Inferring the geostrophic and vertical velocity fields. J. Geophys. Res.: Oceans 101 (C7), 16291–16303. http://dx.doi.org/10.1029/96JC01144.

Lawson, C.L., Hanson, R.J., 1995. Solving least squares problems, second ed. Society for Industrial and Applied Mathematics (SIAM), Philadelphia, PA, pp. 158–173.

Nicholson, J., 2021. Regularizend. https://www.mathworks.com/matlabcentral/fileexchange/61436-regularizend.

Press, W.H., Teukolsky, S.A., Vetterling, W.T., Flannery, B.P., 1992. Numerical Recipes in Fortran 77: The Art of Scientific Computing Volume 1 of Fortran Numerical Recipes, second ed. Cambridge University Press, Cambridge, pp. 863–869.

Tang, C.L., 1980. Observation of wavelike motion of the gaspé current. J. Phys. Oceanogr. 10 (6), 853–860. http://dx.doi.org/10.1175/1520-0485(1980)010<0853:OOWMOT>2.0.CO;2.

Saucier, F.J., Roy, F., Gilbert, D., Pellerin, P., Ritchie, H., 2003. Modeling the formation and circulation processes of water masses and sea ice in the gulf of St. Lawrence, Canada. J. Geophys. Res.: Oceans 108 (C8), http://dx.doi.org/10.1029/2000JC000686.

Levasseur, M., Fortier, L., Therriault, J.-C., Harrison, P.J., 1992. Phytoplankton dynamics in a coastal jet frontal region. Mar. Ecol. Prog. Ser. 86, 283. http://dx.doi.org/10.3354/meps086283.

Mertz, G., El-sabh, M.I., 1989. An autumn instability event in the gaspé current. J. Phys. Oceanogr. 19 (1), 148–156. http://dx.doi.org/10.1175/1520-0485(1989)019<0148:AAIEIT>2.0.CO;2.

Chelton, D.B., Esbensen, S.K., Schlax, M.G., Thum, N., Freilich, M.H., Wentz, F.J., Gentemann, C.L., McPhaden, M.J., Schopf, P.S., 2001. Observations of coupling between surface wind stress and sea surface temperature in the eastern tropical Pacific. J. Clim. 14 (7), 1479–1498. http://dx.doi.org/10.1175/1520-0442(2001)014<1479:OOCBSW>2.0.CO;2.

Koutitonsky, V., Bugden, G., 1991. The physical oceanography of the gulf of St. Lawrence: A review with emphasis on the synoptic variability of the motion. In: The Gulf of St. Lawrence: Small Ocean or Big Estuary? Canadian Special Publication of Fisheries and Aquatic Sciences. vol. 113, pp. 57–90.

Kobashi, D., Hetland, R., 2020. Reproducibility and variability of submesoscale frontal eddies on a broad, low-energy shelf of freshwater influence. Ocean Dyn. 70 (11), 1377–1395. http://dx.doi.org/10.1007/s10236-020-01401-4.

Thomas, L.N., Joyce, T.M., 2010a. Subduction on the northern and southern flanks of the gulf stream. J. Phys. Oceanogr. 40 (2), 429–438. http://dx.doi.org/10.1175/2009JPO4187.1.

Thomas, L.N., Lee, C.M., Yoshikawa, Y., 2010b. The subpolar front of the Japan/east sea. Part II: Inverse method for determining the frontal vertical circulation. J. Phys. Oceanogr. 40 (1), 3–25. http://dx.doi.org/10.1175/2009JPO4018.1.